Compositional Characterisation of Skarn Garnet in the Pernatty Lagoon Region, and Comparisons with Punt Hill and Hillside

Thesis submitted in accordance with the requirements of the University of Adelaide for an Honours Degree in Geology

Cameron Macphail

October 2017

THE UNIVERSITY
of ADELAIDE

ABSTRACT

The Pernatty Lagoon Region is located on the eastern margin of the Gawler Craton, within the Stuart Shelf of South Australia. The Gawler Craton is host to a range of sub-economic garnet skarn systems, within Pernatty Lagoon is the PLR21/SAR8 drill hole which is characterised by heavy skarn-style alteration with a uniform mineralisation halo (Cu–Pb–Zn). Punt Hill and Hillside both reside within the Wallaroo group lithological package of the Gawler Craton approximately 6km East and 380km South of Pernatty Lagoon respectively, allowing for a proximal/distal comparison to be drawn. Laser–ablation inductively–coupled plasma mass spectrometry spot analyses and grain scale element distribution mapping determines the concentrations of rare earth elements/incompatibles and their distribution at grain scale. Garnets from SAR8 fall into the grandite range from $And_{99-85}Gr_{0-13}Sp_{1-2}$ to $And_{74-56}Gr_{23-41}Sp_{1-2}$. Laser–ablation inductively–coupled plasma mass spectrometry spot analyses and grain scale element distribution mapping show Gawler Craton garnet skarns are unique to other skarn garnet deposits as they are high in $\sum$REE+Y and U, have similar garnet compositions, a unique REE+Y distribution (cores enriched in light rare earth elements (LREE), flat heavy rare earth elements (HREE) and rims with similar LREE to HREE, only severely depleted in lanthanum and cerium), and an enrichment in W, Sn, As and Cr. YAG–style REE+Y fractionation only partly accounts for the distribution of REE+Y patterns. X-site ionic radii substitution accounts for the unusual LILE fractionation, with Cl^- and F^- complexes being a major suppository of La^{3+} within hydrothermal fluids. The suggested potential for W, Sn, As and Cr enrichment as a vector for mineralisation and fluid flow is rendered inconclusive, instead the enrichment is due to host rock compositions associated with the fluid pathways.

KEYWORDS

Skarn, garnet, IOCG, Pernatty Lagoon, Punt Hill, Hillside, mineral trace elements.

CONTENTS

LIST OF FIGURES AND TABLES

INTRODUCTION

The Eastern Gawler Craton hosts over 600km of arcuate Iron Oxide–Copper–Gold (IOCG) mineralisation, otherwise known as the Olympic Province (Reid *et al.*, 2017). This belt is host to not only the Olympic Dam world class deposit and many significant deposits such as Prominent Hill, but also a large extent of sub-economic mineralisation Reid & Fabris, 2015; Morrissey *et al.,* 2016). The Pernatty Lagoon mineralisation prospect is hosted within calcic exoskarns of sedimentary protolith (Payne *et al.,* 2006).

The comparison between the mineralogy and geochemistry of unaltered rock regions compared with their equivalent altered, mineralised regions is vital in tracking the evolution of an ore system (Harrow and Skirrow, 2010). This can be used to distinguish between local versus regional signatures of mineralisation footprints, and together with comparisons to other areas, will contribute to determining a structural framework for fluid sources and alteration distributions (Bastrakov et al., 2007; Skirrow *et al.*, 2007; Conor *et al.*, 2010; Kontonikas-Charos *et al.*, 2014; Fabris *et al.,* 2016; Reid *et al., 2017).*

The Olympic Province is almost entirely buried underneath hundreds of metres of cover, yet has yielded significant amounts of the world's copper, gold and uranium supplies. This renders conventional exploration methods difficult, and often ineffective. The Stuart Shelf region, which contains Pernatty Lagoon and the surrounding areas (Figure 1A), has been sporadically drilled (Figure 1B) with mostly sub economic to economic mineralisation encountered, but has provided enough geochemical data to potentially constrain the alteration, and therefore vector successful ore systems (Bastrakov, 2007; Davidson *et al.,* 2007; Reid *et al.,* 2011; Ismail *et al.,* 2014; Fabris *et al.,* 2016).

Pernatty Lagoon is located along the eastern margin of the Gawler Craton, South Australia. Oxidized (magnetiteseries), A- to I-type granitoid plutons of the 1595–1575 Ma Hiltaba Suite (Morrow & McPhie, 2000; Allen *et al.,* 2003; Payne *et al.,* 2008), and largely coeval

intermediate to mafic volcanic rocks of the lower Gawler Range Volcanics (GRV) (Reid & Fabris, 2015), representing an intracontinental magmatic province (Hand *et al*., 2007).

Garnet is an excellent host of Rare Earth Elements (REE), which can be used to indicate proximal from distal to ore assemblages/fluid origin (Gaspal *et al*. 2008). As a refractory mineral, it is useful in indication prograde and retrograde events, including PT paths and alteration events (Nicolescu *et al.,* 1998; Otamendi *et al.,* 2002; Peng *et al.,* 2015; Raimondo *et al.,* 2017).

This study considers variation in garnet geochemistry as a function of depth compared to copper, zinc and lead mineralisation to derive correlations between the element distribution preference in garnet growth and zonation vs. whole rock geochemistry. Similar studies have been undertaken in Punt Hill (Nikolakopoulos, 2013) and Hillside (Ismail, 2014), so comparisons between garnet geochemistry will allow for a development of skarn hydrothermal fluids and systems. Enrichment in W, Sn, As and Cr within garnet is a potential vector for mineralisation and fluid flow, coupled with unique REE variations and magnitudes.
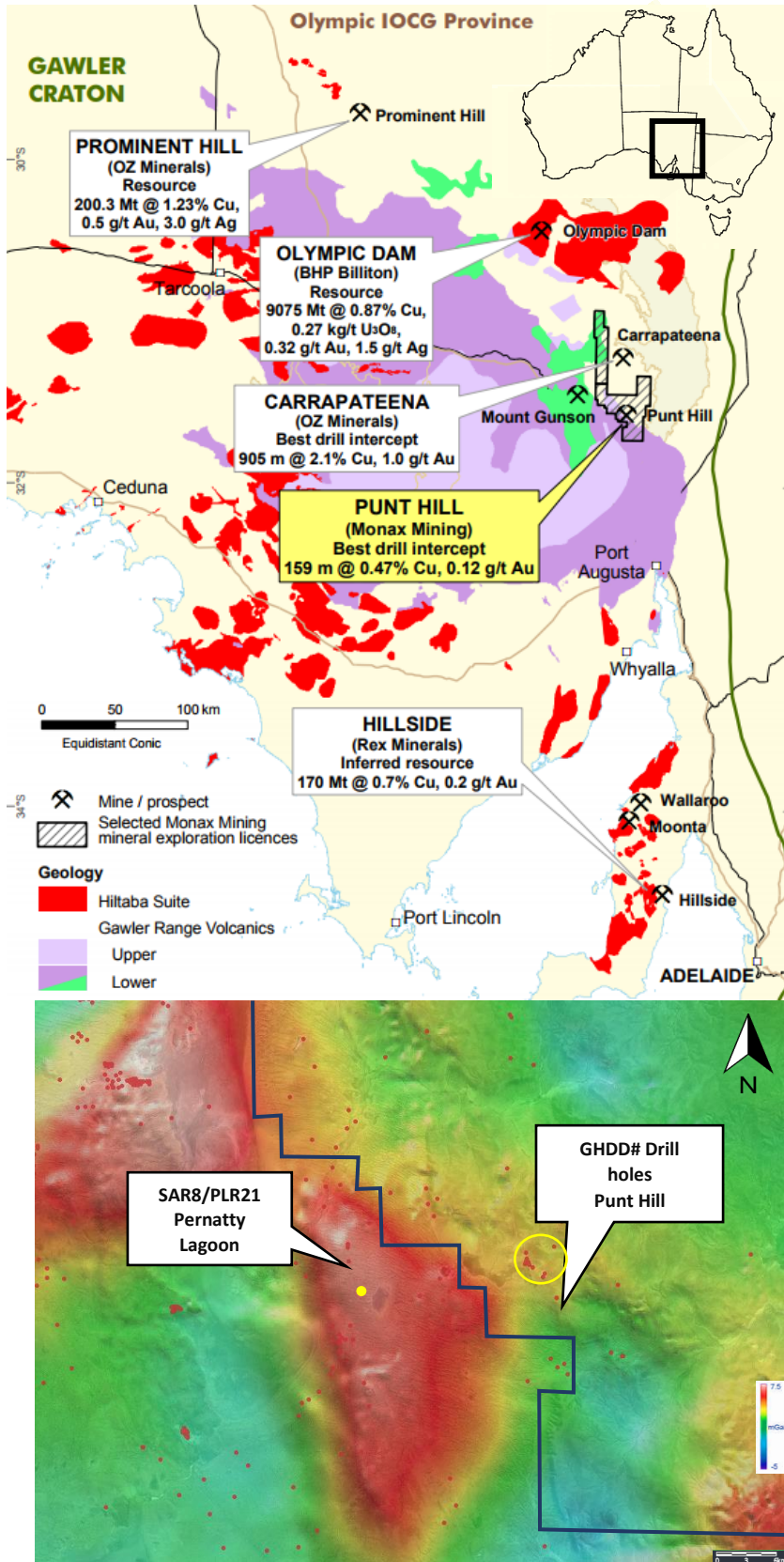
Figure 1: A) Interpreted geology of the Eastern Gawler Craton, showing the location of Hillside and Punt Hill, and other prospects. Adapted from (Reid et al., 2011). Pernatty Lagoon is located 16km east of Punt Hill. B) Gravity geophysical data over the Pernatty Lagoon/Punt Hill area establishing the spatial relationship between the two study areas. Red dots indicate locations of other drill holes in the region, sporadically distributed.

GEOLOGICAL SETTING

Pernatty Lagoon is located within the South Australian Olympic Province (Figure 1A), on the arcuate eastern margin of the Gawler Craton which extends over 600km containing numerous prospects alongside Olympic Dam and Prominent Hill (Ferris et al., 2002; Hayward and Skirrow, 2010; Skirrow et al., 2002, 2007). The Gawler Craton basement is comprised of 3150Ma Archean granite and the Sleaford and Mulgathing Complexes (Swain *et al.,* 2005*)* overlain by Paleo–to Mesoproterozoic volcanic and metasedimentary rocks. These rocks have been subject to protracted crustal growth and tectonic history, of which two deformation events are uniformly recognised, the emplacement of the magmatic Donington Suite (1850 Ma) and the Kimban Orogeny (1730–1690 Ma) (Hand et al., 2007; Reid and Hand, 2012). The skarn mineralisation is within the 1760–1740 Ma Wallaroo Group. Alteration and associated IOCG mineralisation within the Olympic Province formed between ~1570 and ~1600 Ma (Skirrow et al., 2007, Ciobanu et al., 2013) which overlaps with magmatism (Hilltaba and GRV) based on hydrothermal mineral geochronology. Reid (2011) reported a garnet–diopside whole rock Sm–Nd isochron of skarn mineral assemblage formation at Punt HillGarnet–diopside aggregates make up the majority of the Pernatty Skarn.

The SAR8 drill hole was drilled on a positive gravity anomaly following subsequent sub-economic prospects drilled in the area. From 996.5 metres, the rock is a laminated siltstone breccia which becomes progressively more altered and veined by epidote and actinolite down hole. From 1012 metres it becomes brecciated, comprised of red–brown angular siltstone/chert clasts, in a pale green chlorite/epidote/actinolite/carbonate matrix. The core is mineralised from 1014 to 1218 metres, containing pyrite, chalcopyrite, sphalerite and minor galena. Grossularite and fluorite are sporadically present as patches, and brecciated, slumped and laminated chert and siltstone bands are common. The sulphides generally occur as finely disseminated grains and occasionally aggregates. Veinlets of sphalerite, chalcopyrite and

pyrite with carbonate, fluorite is common in exceptionally mineralised portions. From 1218m

sulphides become significantly less abundant with decreasing garnet in the matrix.

Brecciation also decreases until it becomes a laminated siltstone with strong hematite

alteration at 1284 metres, continuing until the end of the hole.
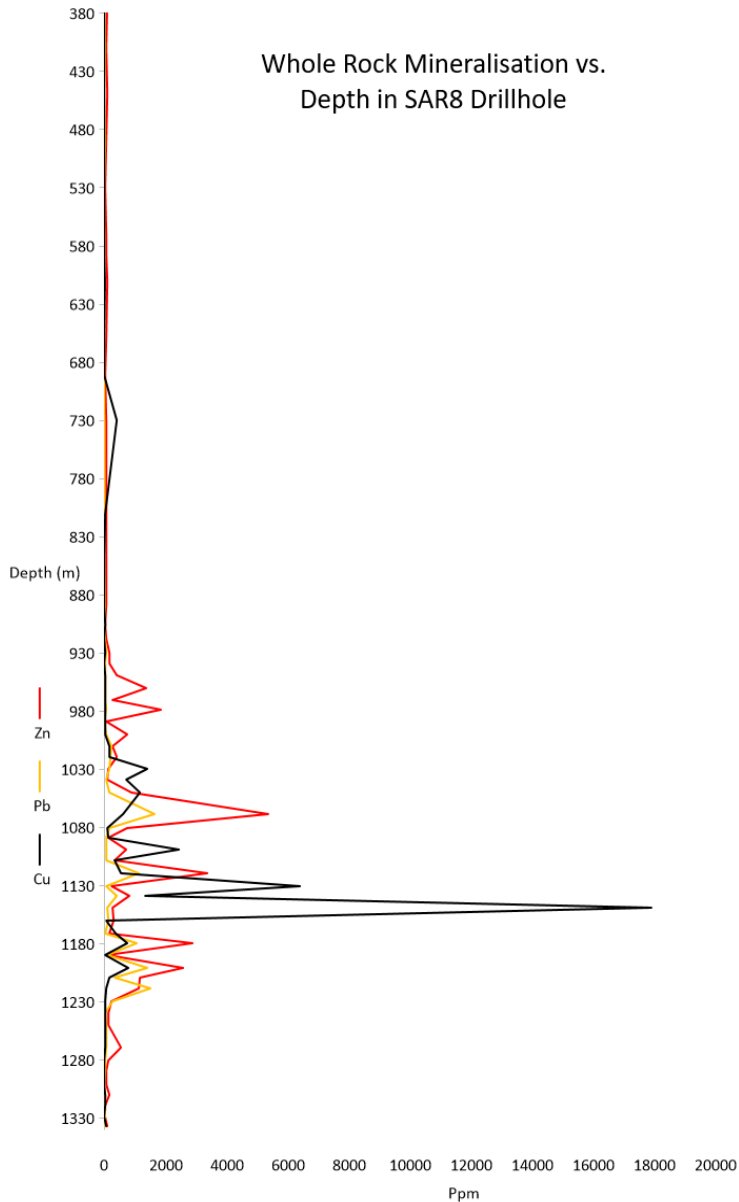
Figure 2: Whole rock geochemical data from Fabris (2016) as a function of Depth in the SAR8 Drill hole. This is the zone of mineralisation that this study has used to analyse garnet geochemistry. Grid coordinates of SAR8 are 723550E 6502906N (Map Grid of Australia 1994 (MGA94), Universal Transverse Mercator, using the GRS80 ellipsoid)

11
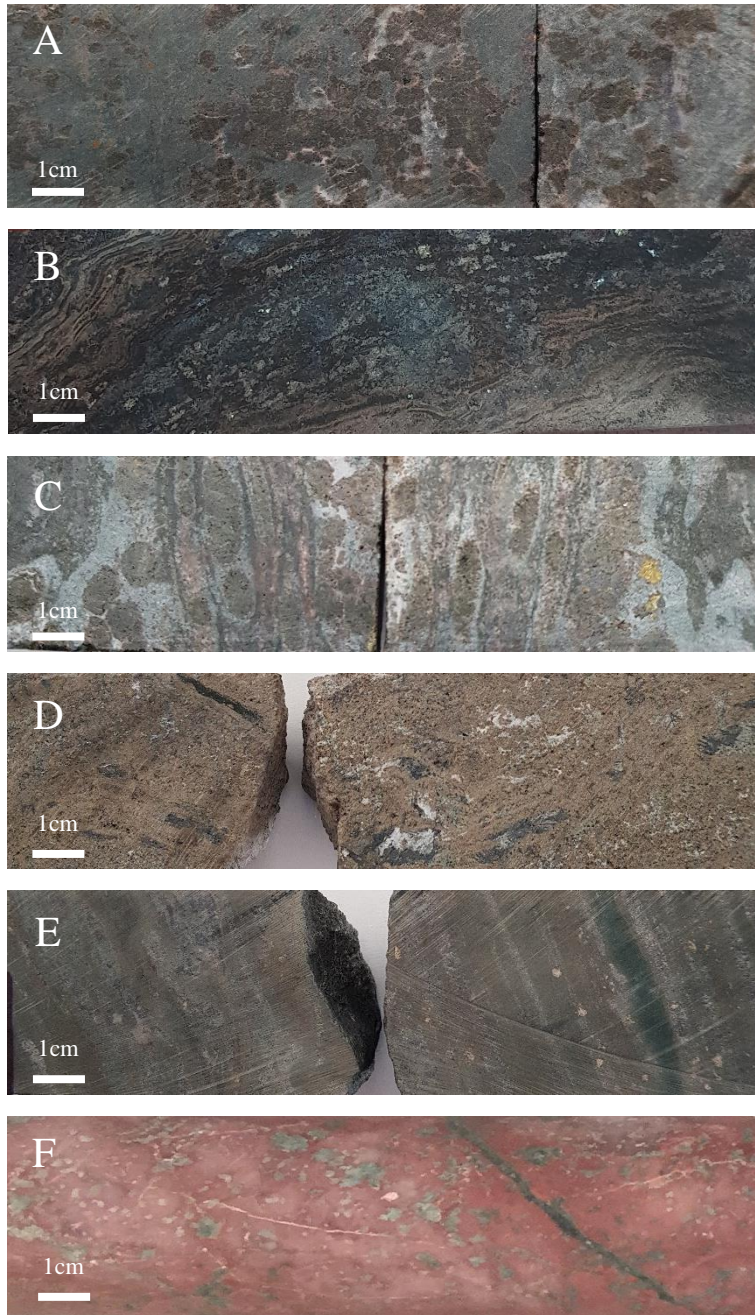
Figure 3: Photographs of hand-specimens of typical lithologies in SAR8. A) 1108.4m depth. Garnet-pyroxene-calcite-chlorite skarn altered silicate rock with calcite-quartz-anhydrite fracture fillings. Abundant closely packed subhedral garnet grains ~0.5 – 5mm comprise most of the rock (<75%). Calcite occurs as fine interstitial patches and chlorite as very fine grained pervasive alteration of garnet. B) 1148.7m depth (peak copper mineralisation). Garnet-sulphide-actinolite-hematite skarn altered rock. Distinct laminations of garnet, actinolite and hematite are present, with chalcopyrite, pyrite and sphalerite present as ragged grains and aggregates/discordant patches intergrown with minor K-feldspar. C) 1170.85m depth. Garnet-pyroxene-sulphide skarn altered silicate rock with weak calcite retrogression. Yellow garnet is overgrown by paler yellow/brown garnet. Most calcite from anhedral grains in between garnet crystals, with some occurring as fine grain replacements of euhedral crystals within garnet grains. D) 1138.8m depth. The most common mineralogy and textures present in SAR8. Garnet-pyroxene-actinolite-calcite skarn altered silicate rock. Garnet is abundant (<70%) occurring as dark yellow with occasional pale yellow/brown cores. Pyroxene is pale green with actinolite/calcite/quartz occurring as late forming infill. E) 1261.1m depth. Unmineralised laminated siltstone breccia. F) 1235.5m depth. High intensity hematite-quartz-K-feldspar altered breccia.

The protolith to the skarn in SAR8 would have formed as a fine-grained sediment. However, no primary minerals or textures from the original protolith are present after the skarn-type replacement by garnet. The dark yellow to pale yellow/brown colour suggest the garnet grains are grossular to andradite (grandite range), and the abundance suggests that this alteration event was at elevated temperatures. The infilling of calcite–quartz ± anhydrite–sulphides (e.g. Figure 3 A–D) indicates a different hydrothermal fluid entered through brittle fracturing. The euhedral crystals, coupled with minor quartz vugs suggest that this event

12

occurred at comparatively low temperatures. Lamination of alteration minerals (e.g. Figure 3B) likely reflects precursor primary lamination. Sulphide formation belongs to the later stage of metasomatic alteration along with chlorite, calcite and rare hematite. "Red rock" alteration (e.g. Figure 3F) is a prevalent mineralogy throughout the Gawler Craton, although is not present in the mineralised portion of SAR8. However, it does indicate the oxidised oxidation state of the drill hole.

The main comparative studies for this study were conducted at Hillside (Ismail, 2014) and Punt Hill (Nikolakopoulos, 2013). Together with this study, the previous work can be used to create an Atlas like representation of skarn mineralisation across the Eastern Gawler Craton. Previous studies were conducted across a series of drill holes that were in close proximity to each other, using marker horizons to establish the same stratigraphic levels, and using lateral distance to separate mineralised from non-mineralised region. This project instead focused on one drill hole that featured a very distinct zone of mineralisation to create a direct comparison between garnet geochemistry and whole rock mineralisation. Mineralogy and textural relationship are comparatively similar between all three studies.

METHODOLOGY

Analytical and petrological studies were undertaken on seventeen samples encompassing the mineralised zone in SAR8 of Cu, Zn and Pb (Zn and Pb are analogous). Fabris (*et al.,* 2016) conducted whole rock geochemistry at approximately 10m intervals throughout SAR8 (elements analysed, and determination techniques given in Appendices A). The samples range from non-mineralised (sample 65) to peak Cu (sample 80) and peak Zn (sample 88) then back to non-mineralised (sample 99). These samples are representative of skarn mineralisation and were therefore used to view the garnet geochemistry as a function of whole rock mineralisation.

The samples were prepared as one-inch polished grain mounts hosting chips of the drill hole. These samples were petrologically assessed to identify minerals, significant textures and mineralogical relationships. They were then examined under transmitted and reflected light using a Nikon LV100 polarising microscope.

Of each sample, one garnet was selected as a representative for geochemical analysis. These garnets are named the same as their sample number for continuity. Each garnet has been analysed to obtain major and minor element compositional data using a Cameca SX–Five electron microanalyser (Adelaide Microscopy). Operating conditions, standards, typical minimum detection limits and X-ray lines are given in Appendix A.

Spot data was gathered as transects across garnet grains to show trace element distributions as a function of garnet growth. The spot analysis were collected using Laser–Ablation Inductively Coupled Plasma–Mass Spectrometry (LA–ICP–MS) using the Agilent 7500cx with coupled New Wave UP–213nm Laser Ablation System (Adelaide Microscopy). LA–ICP–MS element distribution mapping was conducted for selected garnet grains of approximately $2mm^2$ to $8mm^2$ to provide a visual distribution at grain scale. Details of the

full analytical methodology for the LA–ICP–MS spot analysis and element mapping are provided in Appendix A.

The data gathered in this project are of current and future interest to the minerals industry with regards to exploration and ore vectoring. Therefore, additional element maps, petrographic images and spot data not included in the main body of this study are presented in the Appendices.

Table 1: Sample suite showing sample ID, depth and whole rock mineralisation values (Fabris, 2013).

Depth (m)	Sample ID	Cu (ppm)	Zn (ppm)	Pb (ppm)
906.3	65	24	38	5
970.6	71	12	258	45
1029.3	77	1394	142	169
1039.1	78	701	114	49
1050.1	79	1164	882	176
1089	82	130	120	49
1099.2	83	2451	722	64
1108.4	84	334	355	60
1119.25	85	552	3373	1140
1130.3	86	6417	247	80
1138.8	87	1347	807	406
1148.7	88	17913	278	84
1160.5	89	52	299	137
1170.85	90	388	163	31
1179.8	91	750	2894	1062
1201	93	798	2571	1394
1269.3	99	12	546	53
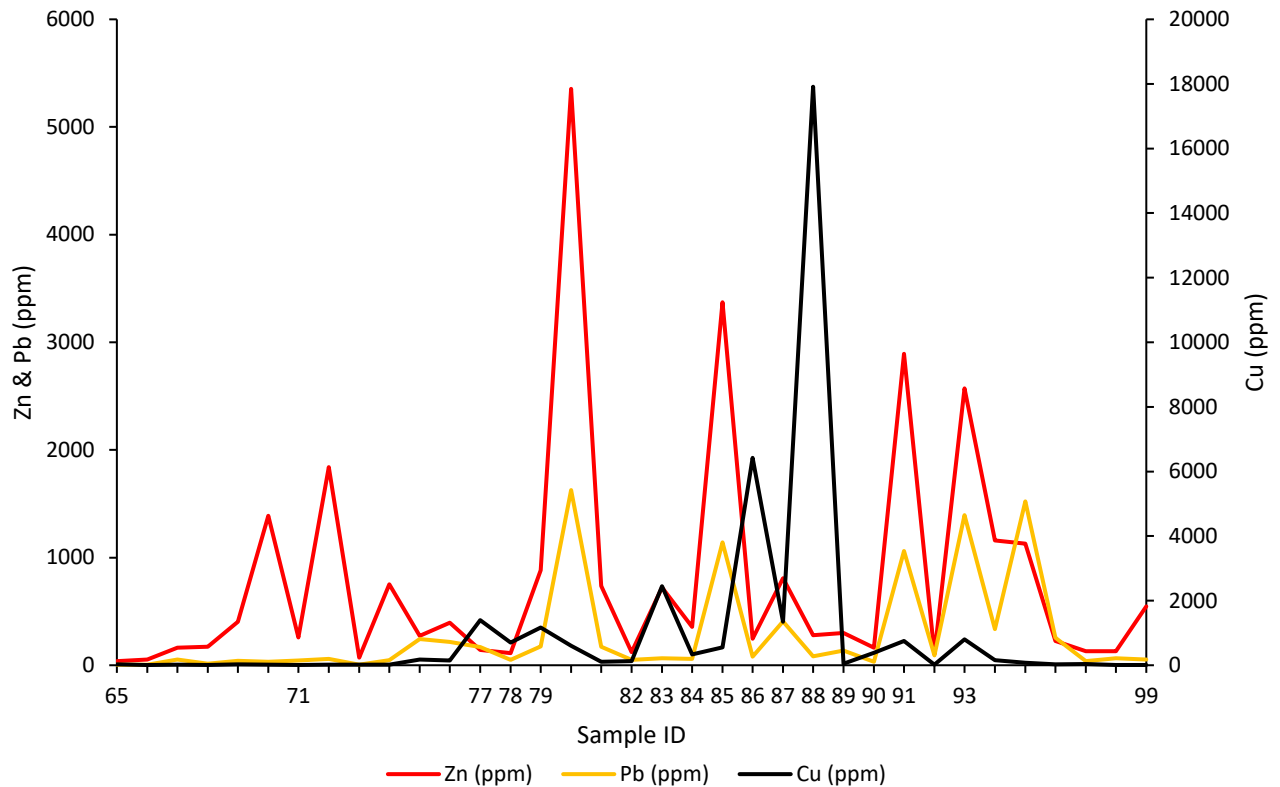
Figure 4: Whole rock mineralisation values (Fabris, 2016) for each sample, peak mineralisation for Zn and Cu occur at samples 80 and 88 respectively.

OBSERVATIONS AND RESULTS

Petrography

Garnet skarn (where garnet > pyroxene) dominates the SAR8 mineralised horizon. There is no relationship between the abundance and size of garnets, although, before and after the mineralisation depth the abundance percentage of garnet strongly decreases. Texturally garnet can co–exist, cut and replace other minerals and *vice–versa*. The matrix of the skarn is typically fine grained (<2mm) consisting of amphibole, quartz, chlorite, talc, carbonates and occasional fluorite. Accessory minerals include zircon, titanite and relatively abundant apatite, which is found as inclusions within garnet.
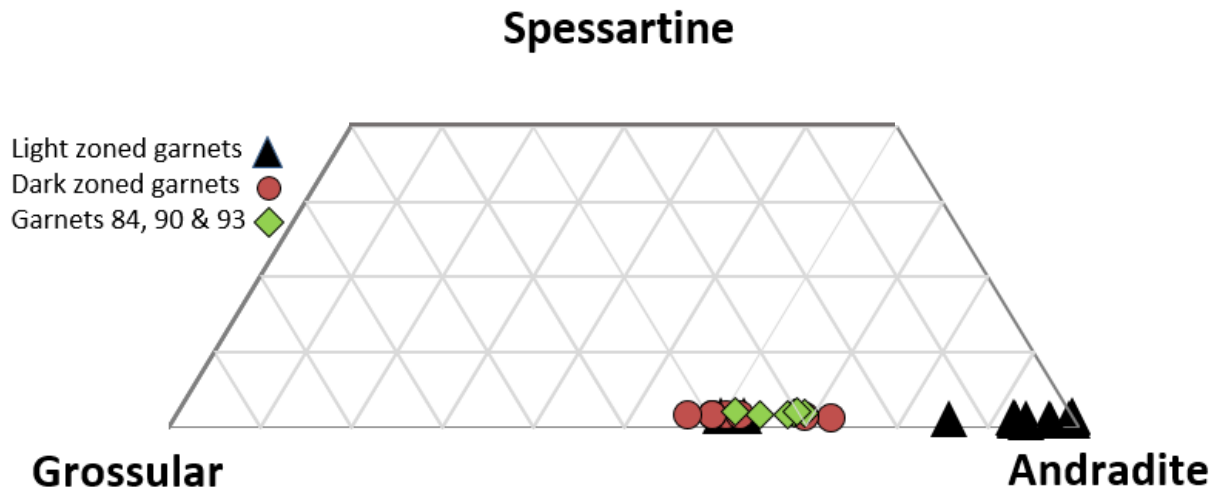
Figure 5: Ternary compositional plot for all garnets, expressed as functions of andradite, grossular and spessartine end–members. Data is compiled from electron probe microanalyzer (EPMA) results on all garnets in SAR8. Light zones of garnets consist mostly of the cores of the grains, and are almost entirely andradites. Dark zoned garnets mostly consist of the rims and are depleted in Fe and enriched in Al. Garnets 84, 90 and 93 are compositionally consistent throughout the grain, and there is very little difference between the cores and rims of these grains, aside from a tendency for the cores to be light zoned. A correlation can be inferred indicating an early, prograde enrichment in Fe progressing into an Al-rich retrograde stage.
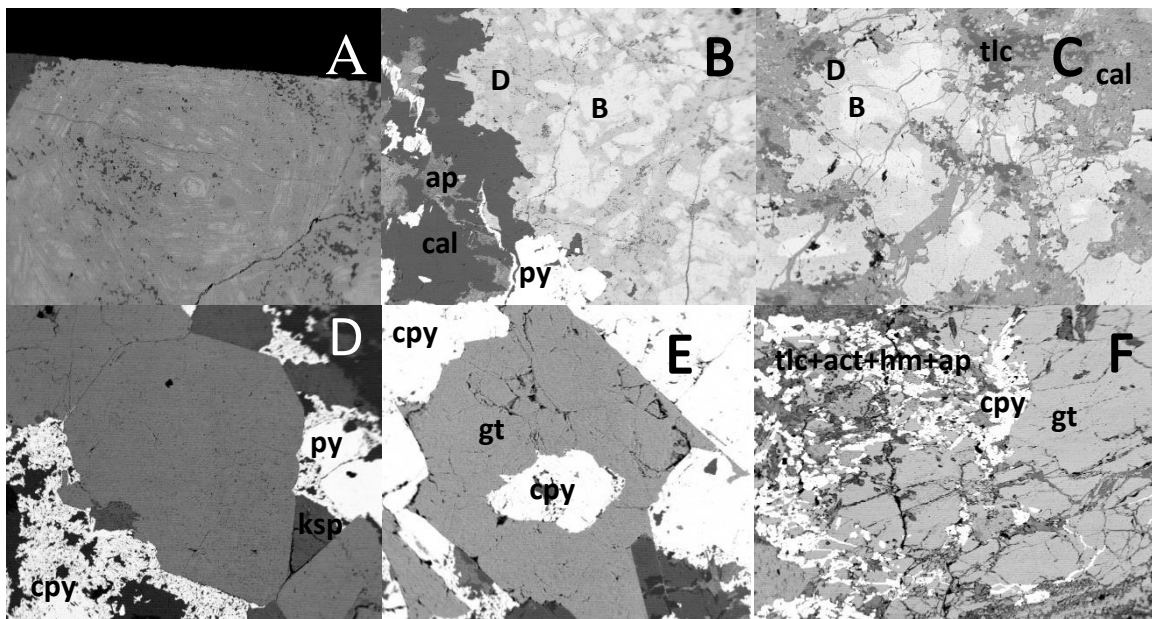
Figure 6: BSE images of various garnet grains and textural relationships. A) Type I garnet sample 90 highlighting the oscillatory zoning between dark and light zones. B) Type II garnet sample 89 showing the weakly zoned relationship between dark zones (type D) and light zones (type B). Apatite (ap), calcite (cal) and pyrite (py) comprise the matrix of in the Pernatty Lagoon mineralised skarn. C) Type II garnet sample 77 showing extreme brecciation of a grain, causing zonation between dark zones (D) and light zones (B) around matrix inclusions of calcite and talc (tlc). D) Garnet sample 84 displaying no colour zonation within the garnet grain, with EMPA results yielding almost no change in composition from rim to core. Infill accessory minerals of potassium feldspar (ksp), chalcopyrite (cpyl) form a district boundary relationship with the garnet, and are present with dusty Fe–oxide inclusions. E) Chalcopyrite occurring within the garnet (sample 90) grain (gt) and around it, indicating texturally two separate stages of sulphide deposition and therefore two separate mineralisation events. F) Ore petrology relative to classic brecciated skarn in Pernatty Lagoon. Talc and apatite are intergrown with actinolite (act) and hematite (hm). Disseminated sulphides and calcite are spread throughout the matrix as well, with brecciated garnet accounting for 60% of whole rock.

Skarn garnet textural and compositional variation

Skarn garnets throughout the Wallaroo Group are characteristically varied in texture and composition. Petrological analysis and EMPA data suggests there is no correlation between mineralisation and the style of garnet, instead being influenced by localised host rock and brecciation style allowing for fluid flow. Garnet mineral chemistry has no influence on the texture of the garnet. This also forms no relationship with accompanying mineral phases. EMPA data (appendices A); (Figure 4) show that garnet is represented compositionally by the members of andradite (And), grossular (Gr) and spessartine (Sp) solid solution series with compositions of $And_{99-58}Gr_{0-39}Sp_{1-2}$. This indicates the garnets are within the grandite garnet series.

Two main types of garnet are defined throughout the skarn, "light" zoned garnets (B) and "dark" zoned garnets (D) (Figure 4) which are observed in BSE images due to the differing atomic mass of minerals, which, in the case of these garnets, has been caused due to the large enough difference in end member compositions to show areas of zonation. Light zonation corresponds to enrichment of Fe, with almost all compositions falling within the range of $And_{99-85}Gr_{0-13}Sp_{1-2}$. Dark zonation corresponds to the range of $And_{74-56}Gr_{23-41}Sp_{1-2}$. Garnets 84, 90 and 93 featured no notable zonation and both the cores and rims fall within the compositional range of dark zoned garnet.

While light and dark zonation patterns are present in the majority of garnet grains, the composition of the garnets, these can broadly be divided into two sub-types; oscillatory zoned garnets (type I), which usually contain a light zoned core and dark zoned rim, and weakly zoned garnets that rarely show any trend between core/rim zonation, and are often inclusion rich (type II). The different types of garnet are shown in Figure 4.

Skarn mineralisation

SAR8 is a sub-economic drill hole with peak base metal concentrations peaking at 3.2% Cu,
1.3% Zn and 0.4%Pb. Economic minerals are chalcopyrite, chalcocite, bornite, sphalerite and
galena, with minor components of fahlore, wittichenite and native silver. Sulphides occur as
patches of up to 6mm, and within veins and disseminations over the interval of 940m to
1240m depth. The greatest sulphide concentrations occur at depths of 1079m and 1149m,
respectively. Chalcopyrite and sphalerite are the most common sulphides (with minor galena)
and mostly occur within the matrix. Rare replacement of garnet by sphalerite/galena is
present, and some replacement of garnet via inclusions that form skeletal growth parallel to
compositional zoning (Figure 4E). Two stages of sulphide deposition/mineralisation can be
inferred via textural relationships and whole rock geochemical data; early Zn±Pb
(replacement of garnet) and late Cu±Zn–Pb (co-existing with and post-dating garnet rims).

Concentrations and Distributions of Trace Elements in Garnet and Accessory Minerals: LA–ICP–MS Data

Rare Earth Elements (REE) were analysed via ICP–MS and normalised to the chondrite
values of McDonough and Sun (1995). Yttrium was included between Dy and Ho as a
pseudolanthanide (Bau & Dolski, 1995). Each garnet sample displays distinct REE patterns,
and changes in distribution dependant on separate growth zones. Overall, averages of whole
garnet in the skarn display enrichment in light REE (LREE), with relative, depletion in La
and Ce. Heavy REEs (HREE) are consistently equal, and Eu is either enriched or depleted,
rarely exhibiting normalised values similar to those of Sm and Gd in each garnet. Garnet
exhibits variable patterns and element distribution trends dependant on a range of variables,
with banding as small as several µm. Brecciation is quite sever through the whole skarn
which is reflected in most garnets. Because of this it must be emphasised that inevitable
averaging of compositional variation may have occurred during spot and map analysis.

Rare earth elements and yttrium

Garnet can incorporate significant amounts of REE's throughout any stage of its crystal growth (Smith, 2004; Gaspar, 2008; Ismail, 2014). By doing LA–ICP–MS transects across garnet grains from the seventeen samples, the variety of REE+Y compositions and trends of the system can be determined. Normalising the values obtained to (McDonough and Sun 1995) can therefore be useful in observing the fractionation trends of LREE relative to HREE, assisting in petrogenetic interpretation of this skarn relative to Punt Hill and Hillside.

The average composition of each garnet from each sample (with no differentiation between core and rim) is used to represent a specific depth interval down the drill hole, revealing variations in the REE distribution as a function of distance away from the system. Figure 6 shows that LREE is enriched relative to HREE. The LREEs are curved, with La and Sm being depleted compared to the surrounding lanthanides. A flat slope in HREEs indicates little variation in concentration from Gd to Lu. Variation is greatest from Nd–Sm–Eu, with Sm depleted and Eu often being positively anomalous.

The garnet rims in this system show a flat HREE distribution, with variation in the concentrations of LREE, particularly in depletion of La and Ce in some analyses. Garnet grains in samples 77 and 88 have positive Eu anomalies, whereas almost all other rims have negative Eu anomalies. The negative Eu anomalies coincides with low La and Ce, as highlighted in red in Figure 7. Compared to the average garnet values, the rims have similar ∑REE+Y, differing mostly in the greater degree of depletion of La and Ce, and the Eu anomalies are significantly less in magnitude. Sample 99 is an unusual trend of LREE in comparison to not only the rims, but the averages and cores as well, as La and Ce are enriched comparatively to LREE, leading to a 'bowl' shaped distribution which is a stark difference to the other garnets. It is however, very similar from Nd–HREE concentrations.

Garnet cores show significantly different trends to what is observed in garnet rims, particularly in HREE concentrations. While ∑LREE values show similar variations to the analyses from garnet rims, ∑HREE are increasingly depleted in approximately half of the analyses. The other half of the ∑HREE is similar magnitude concentration to the rims. From Gd to Lu the HREE concentrations have a slight decreasing trend. In Figure 7, the positive Eu anomalies are highlighted in orange and show larger magnitude anomalies than the rims and whole garnet values. La and Ce show the greatest variation among garnet core analyses, but are still in lower concentrations to the corresponding LREEs. Compared to the rims, the LREE distribution trend is more consistent, with most variation resulting from consistent enrichment of REE within individual garnets, as opposed to varying trends in their REE chemistry. Two separate trends exist for the HREEs, one below magnitude 10 from Tb to Er, and the other existing between magnitude 10 to 100 for the same elements. This then differentiates for a more spread distribution for Yb and Lu.

Table 2: Summary of LA–ICP–MS Rare Earth Elements and Trace Elements for Garnet (ppm)

		Y	La	Ce	Pr	Nd	Sm	Eu	Gd	Tb	Dy	Ho	Er	Tm	Yb	Lu	ΣREY		Pb	Th	U
65	Average	43.28	66.91	432.11	78.39	305.36	26.88	10.46	11.12	1.16	7.43	1.59	5.07	0.74	5.20	0.79	996.50		1.46	0.74	107.58
	Rim	132.30	7.49	67.90	15.94	106.60	36.44	6.00	25.03	3.00	21.48	4.84	15.90	2.39	17.28	2.79	465.38		1.69	0.88	24.10
	Core	4.12	103.70	643.00	112.40	410.70	23.40	13.05	4.95	0.28	1.19	0.18	0.38	0.03	0.22	0.02	1317.62		0.69	1.13	156.00
																	0.00				
77	Average	20.14	17.44	72.35	12.35	52.75	6.79	7.64	3.47	0.42	2.96	0.65	2.15	0.30	2.04	0.27	201.73		35.59	5.26	96.48
	Rim	25.50	10.00	48.40	9.40	45.30	6.57	7.13	4.04	0.52	3.76	0.83	2.88	0.39	2.79	0.32	167.82		27.90	7.26	89.80
	Core	8.36	32.00	125.60	18.99	68.00	5.51	9.87	1.98	0.21	1.18	0.26	0.80	0.12	0.84	0.11	273.83		3.61	3.30	155.20
																	0.00				
78	Average	199.13	3.19	26.23	7.16	46.28	20.52	7.41	33.80	6.45	39.52	6.73	16.42	1.99	10.98	1.43	427.24		13.16	2.32	44.05
	Rim	279.50	0.47	3.36	1.43	17.52	20.06	4.81	44.10	9.35	57.10	9.50	21.89	2.36	12.72	1.58	485.75		142.00	3.94	8.25
	Core	28.80	5.51	47.00	13.29	89.20	27.58	12.34	19.03	1.92	7.79	0.94	1.86	0.20	1.08	0.13	256.67		1.09	2.49	75.80
																	0.00				
82	Average	92.44	6.11	49.64	14.30	110.06	43.14	9.35	29.38	3.09	17.11	3.26	9.95	1.38	9.33	1.20	399.76		5.34	10.67	31.04
	Rim	209.30	0.85	9.88	4.51	55.10	37.80	4.73	35.00	4.74	31.26	7.14	25.45	3.67	26.36	3.49	459.29		7.40	10.70	7.13
	Core	52.60	13.66	110.70	29.96	203.70	62.50	19.35	33.80	3.14	13.59	1.90	4.46	0.53	3.04	0.36	553.28		1.58	8.57	50.60
																	0.00				
83	Average	72.10	3.04	40.59	14.69	110.67	31.79	18.35	26.29	3.45	16.83	2.49	5.34	0.59	3.47	0.47	350.16		0.45	2.15	40.07
	Rim	35.80	2.74	47.20	19.40	154.20	31.41	12.64	15.79	1.89	8.99	1.34	2.79	0.33	2.38	0.29	337.19		0.49	0.78	18.10
	Core	48.60	5.19	61.70	20.14	127.00	27.10	20.01	21.40	3.22	13.90	1.89	3.77	0.40	2.13	0.28	356.73		0.29	1.38	57.50
																	0.00				
84	Average	65.47	7.13	33.56	7.29	50.03	19.90	4.87	17.12	2.19	12.33	2.33	6.76	0.93	6.46	0.97	237.34		0.36	0.34	21.14
	Rim	58.17	0.61	9.69	4.56	50.88	24.79	4.19	17.37	2.01	10.93	2.07	6.06	0.83	5.50	0.84	198.50		0.78	0.18	4.83
	Core	8.02	64.60	254.10	36.30	115.20	5.72	9.62	1.38	0.13	0.93	0.25	0.90	0.12	0.92	0.17	498.36		0.37	0.42	136.00
																	0.00				
85	Average	40.44	11.15	84.24	19.75	111.76	27.31	10.95	16.43	1.79	8.96	1.50	3.85	0.48	2.96	0.39	341.96		0.78	3.91	58.28
	Rim	223.00	0.76	7.79	2.61	27.30	25.80	3.93	35.90	5.90	37.90	7.97	24.60	3.45	22.90	3.15	432.96		1.41	2.80	66.30
	Core	3.63	12.41	84.10	17.30	83.50	12.91	8.70	4.04	0.30	1.15	0.15	0.35	0.04	0.17	0.03	228.77		0.63	3.31	66.30
																	0.00				
86	Average	6.92	35.28	66.20	7.13	23.44	2.52	0.38	1.22	0.19	1.04	0.25	0.83	0.14	1.12	0.23	146.89		5.68	8.99	12.08
	Rim	75.00	19.30	121.00	25.00	124.00	20.30	2.48	11.90	2.07	11.40	2.95	8.80	1.34	9.00	1.28	360.82		1.59	8.90	10.90
	Core	1.82	0.40	1.26	0.14	0.54	0.19	0.09	0.31	0.04	0.25	0.06	0.26	0.05	0.41	0.07	5.89		4.56	1.11	2.75
																	0.00				
87	Average	46.55	0.09	2.20	1.39	19.47	18.82	4.10	20.80	1.93	8.36	1.22	2.99	0.41	2.44	0.33	131.08		2.21	0.08	2.80
	Rim	35.16	0.12	2.85	1.61	22.81	18.59	3.72	17.39	1.59	7.43	1.25	3.50	0.45	3.12	0.44	120.02		0.22	0.07	2.84
	Core	34.22	0.11	2.93	1.74	24.76	19.98	4.01	19.82	2.02	10.05	1.70	4.49	0.58	3.79	0.52	130.69		29.20	0.09	3.01
																	0.00				
88	Average	20.45	95.50	399.60	54.80	146.60	4.11	6.93	1.42	0.13	0.70	0.16	0.50	0.07	0.54	0.08	731.59		2.27	7.39	101.95
	Rim	27.20	41.00	216.00	36.30	136.80	8.25	6.59	3.27	0.56	4.07	0.94	2.77	0.35	1.93	0.19	486.22		2.26	10.04	99.50
	Core	4.71	56.37	254.57	38.56	124.58	6.75	6.20	3.19	0.46	3.24	0.71	2.17	0.29	1.86	0.24	503.89		0.76	3.24	138.50
																	0.00				
89	Average	45.10	90.62	15.42	65.20	10.00	6.74	7.94	1.14	7.05	1.37	3.92	0.51	3.29	0.45	0.45	259.20		5.88	1.73	67.39
	Rim	84.40	9.70	52.60	10.60	53.40	11.31	5.91	11.68	1.82	12.06	2.32	7.02	0.94	6.09	0.82	270.67		6.40	4.08	56.90
	Core	75.10	2.21	17.57	5.16	36.40	9.75	4.60	9.68	1.57	10.57	2.29	6.84	0.91	6.01	0.86	189.52		8.20	1.42	22.20
																	0.00				
90	Average	52.30	0.07	1.45	0.91	13.91	16.03	3.82	24.08	3.04	14.25	1.93	4.27	0.47	3.03	0.40	139.99		0.36	0.09	3.57
	Rim	94.70	0.04	1.12	0.77	11.53	14.73	3.79	27.28	4.84	25.35	3.46	7.01	0.72	4.27	0.56	200.17		0.15	0.07	3.39
	Core	35.10	0.07	1.94	1.28	18.24	18.29	3.87	21.23	2.18	8.76	1.23	3.09	0.39	2.45	0.34	118.46		0.09	0.12	4.07
																	0.00				
91	Average	24.66	12.55	97.72	22.94	123.62	27.94	10.86	17.19	1.73	7.24	0.94	1.84	0.17	0.83	0.08	350.32		5.62	6.26	67.28
	Rim	28.50	7.13	68.10	19.57	134.80	39.60	12.10	22.19	2.06	8.52	1.02	2.18	0.22	1.16	0.11	347.26		8.42	9.49	57.70
	Core	0.19	19.41	136.70	27.19	108.80	9.10	9.11	1.36	0.05	0.09	0.01	0.02	0.00	0.00	0.00	312.03		0.20	0.15	77.20
																	0.00				
93	Average	109.96	0.48	6.53	3.34	42.00	32.76	5.92	30.36	3.89	21.72	4.05	11.94	1.69	12.23	1.87	288.75		6.52	2.16	5.55
	Rim	47.90	0.25	5.68	3.07	37.80	22.63	4.40	17.40	1.99	10.24	1.79	4.95	0.65	4.68	0.65	164.09		4.41	1.30	5.76
	Core	27.82	0.10	2.16	1.33	17.41	16.29	3.53	18.04	1.76	7.32	1.03	2.57	0.32	2.30	0.33	102.29		12.00	0.80	4.98
																	0.00				
99	Average	44.59	4.25	15.71	3.83	26.65	11.44	8.81	12.46	1.70	9.23	1.64	4.43	0.59	3.86	0.56	149.75		4.87	2.66	35.17
	Rim	41.90	22.70	28.70	2.97	16.19	14.25	8.36	19.48	2.43	10.84	1.56	3.88	0.44	2.85	0.36	176.90		7.63	5.69	10.18
	Core	5.05	1.31	16.00	5.47	37.67	8.25	10.07	2.57	0.16	0.70	0.16	0.55	0.10	0.70	0.12	88.89		0.40	0.80	56.90
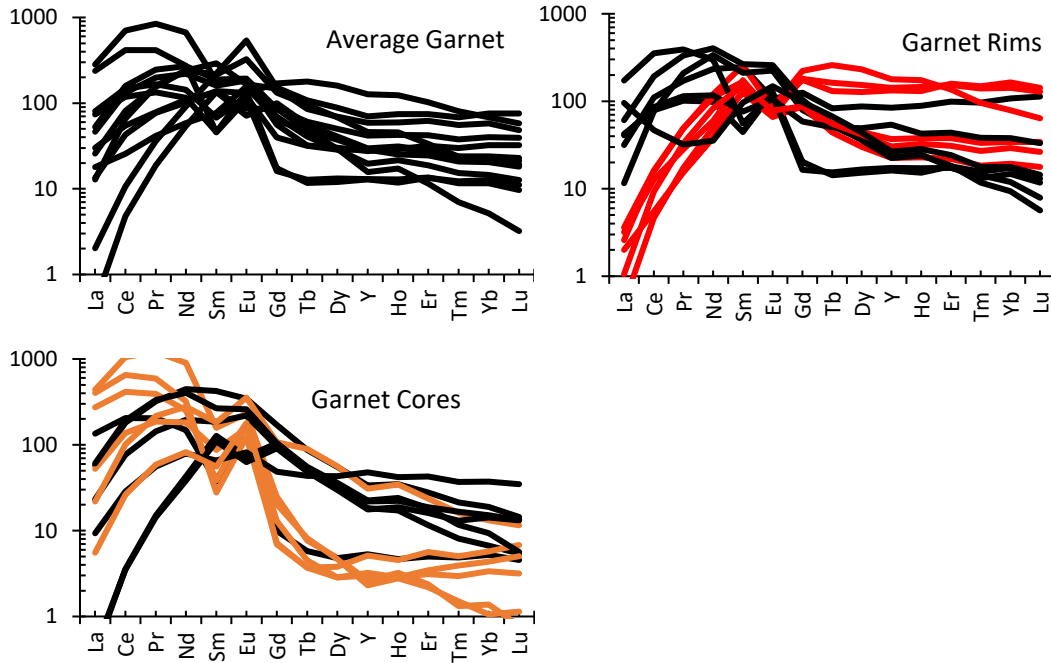
Figure 7: Chondrite normalised REE+Y fractionation trends for all garnets. a) REE+Y chondrite data taken as an average value from all points transecting the individual garnet. b) REE+Y chondrite data from the rims of the garnets, taken as an average of the rim spot data for each garnet in each sample. La depleted garnets are highlighted in red c) REE+Y chondrite data from the cores of the garnets, showing the prograde REE+Y values. Garnet cores containing a positive Eu anomaly highlighted in orange.
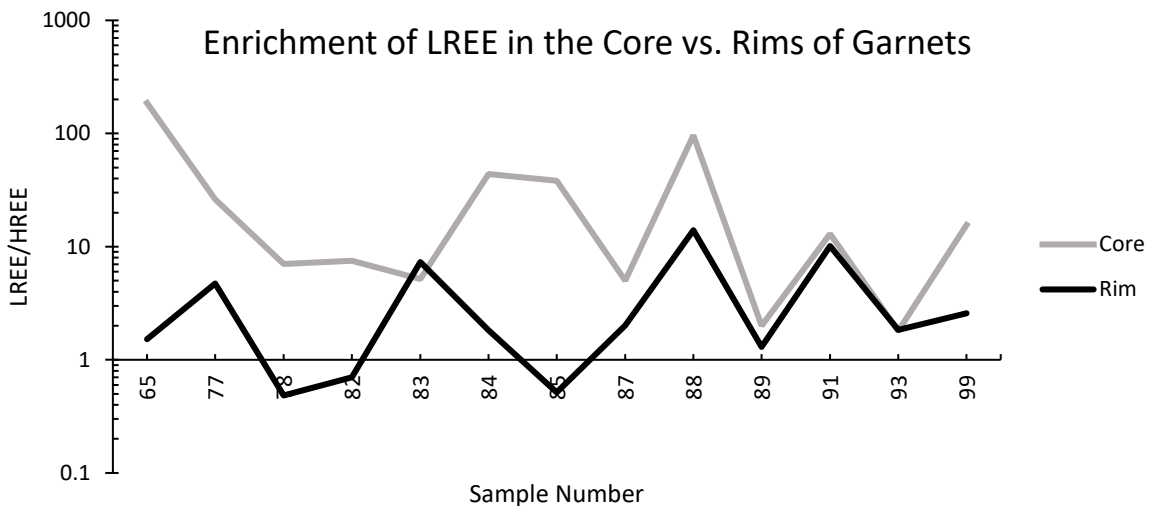
Figure 8: Enrichment of LREE relative to HREE in the cores and rims of each garnet. In general garnets preferentially uptake HREE in the core and LREE in the rim, however within Pernatty Lagoon most garnets are enriched in LREE within the core and HREE within the rims.

Other trace elements

A wide variety of trace elements were analysed to assess the genetic correlation and to

determine whether mineralisation had any notable effect on garnet geochemistry. The skarn

garnets in Pernatty Lagoon are enriched in W, U, Sn and As. However, within this system

there is no notable correlation between mineralisation and any element concentration in the

garnets (Appendix A). Figure 11 is used as a reference to the typical enriched elements vs.

depth.
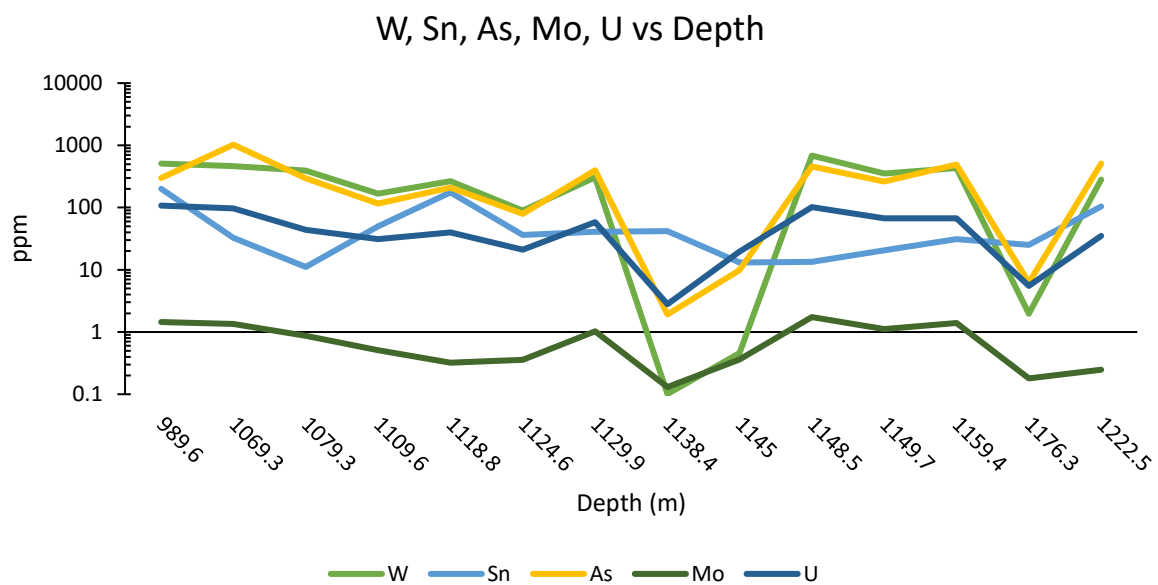
Figure 9: LA–ICP–MS spot data from SAR8. Elements of high abundance in the Hillside and Punt Hill studies, with reference to depth. There is no trend observable.

LA–ICP–MS element distribution maps

The structure of garnet allows minor and trace elements to be distributed throughout the grain

in a wide variety of patterns depending on the conditions of its growth. Major elements are

considered to reflect retrogression/alteration processes as they are less compatible compared

to trace elements and therefore more susceptible to re-equilibrium in the rims from later

occurring conditions. Element distribution maps were collected to explore the trends

developed in the garnets as a function of mineralisation, and as such were created for garnets

at regular intervals in the drill hole. Compositional maps were generated for the following

elements for each garnet: **Ag, Al, As, Au, Ca, Ce, Co, Cr, Cu, Dy, Er, Eu, Fe, Ga, Gd, Hf,**

Ho, K, La, Lu, Mg, Mn, Mo, Nb, Nd, Ni, P, Pb, Pr, Sb, Sc, Se, Si, Sm, Sn, Tb, Th, Ti, Tm, U, V, W, Y, Zn, Zr. Of these elements, Ag, Au, Cu, Zn, Se, Si, P and Mo rarely showed any zonation preference within the garnets. Presented in the main body of this study are only a select few elements for each garnet to avoid unnecessary complication. LA–ICP–MS distribution maps for particular REEs are emphasised upon in this study, as trends in these particular elements were found most interesting. Data for the other elements mentioned can be found in Appendix A.

Many of the garnet grains show a preference for LREE over HREE in the core (Figure 12). This is uncommon, as garnet grains are commonly enriched in HREE in the core. To explore the relationship between element partitioning and garnet growth throughout the mineralised halo, a variety of different garnet types were analysed in terms of their compositions with respect to their spatial relationship to mineralisation.Three type I oscillatory zoned garnets were chosen, two with LREE enriched cores (garnets 87 and 89) and one garnet with a HREE enriched core (garnet 83). Garnet 91 is a type II weakly zoned garnet that features a LREE enriched core to observe partitioning in this type of garnet. In the type I LREE enriched core garnets, LREE are extremely enriched in the cores, whereas HREE are distributed more evenly throughout the grain, reaching peak enrichment in the rim (aside from 87 where peak enrichment is in both the core and rim).

Incompatibles/HFSE (Nb, Sc, V and Ga) may display considerable oscillatory zoning, with the rim in most cases accounting for the greatest concentrations. Ti, Cr and Sc and to a lesser extent Th display enrichment in thin outer layers of oscillatory zoned grains.

Figure 13 provides insight into the effects of brecciation on particular element concentrations. The concentrations of highly compatible elements such as REE+Y are negligible, but the

concentrations of incompatible elements, as well as Cu, Zn, Ti, Cr are strongly influenced.

Interestingly, this zoning has no influence on Sn, U or W.
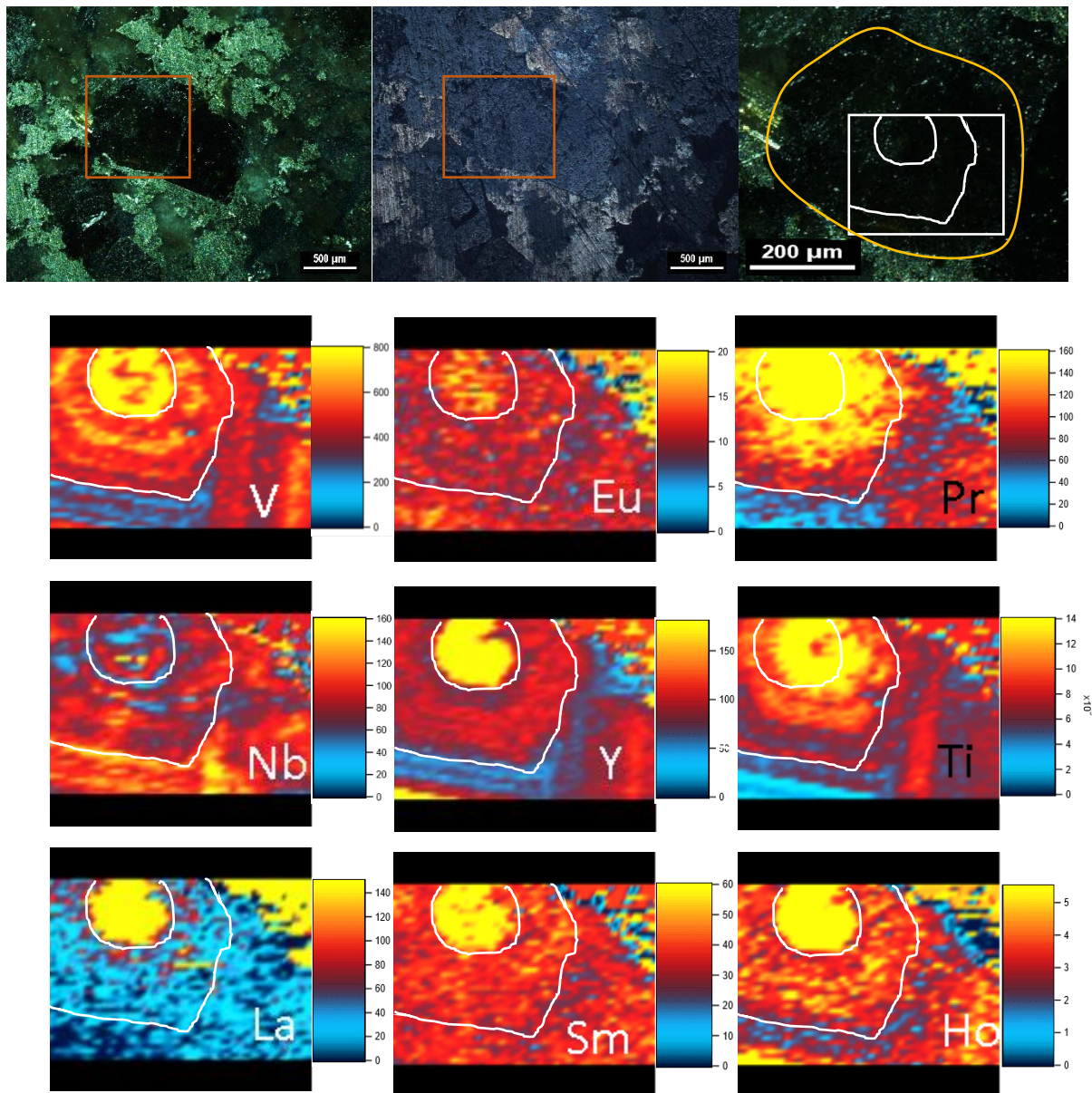
Figure 10: LA–ICP–MS element distribution maps for garnet 87, which is representative of mineralised regions of the skarn. The first image is transmitted light, the second image is reflected light and the orange box highlights the garnet grain. The third image is of the garnet grain, with the yellow highlighting the grain boundary, and the white box showing the element map area and zonation of the elements displayed in the element maps below. Vanadium shows brilliant zoning of elements, from the enriched core oscillatory zoning outwards as concentrations deplete. Both HREE and LREE are enriched in the core as opposed to the rim, but the degree of depletion strongly varies between elements. Nb shows depletion in the core, and enrichment in the rim. Concentrations are given in ppm. The core/middle/rim relationship is highlighted in white on the V element map.
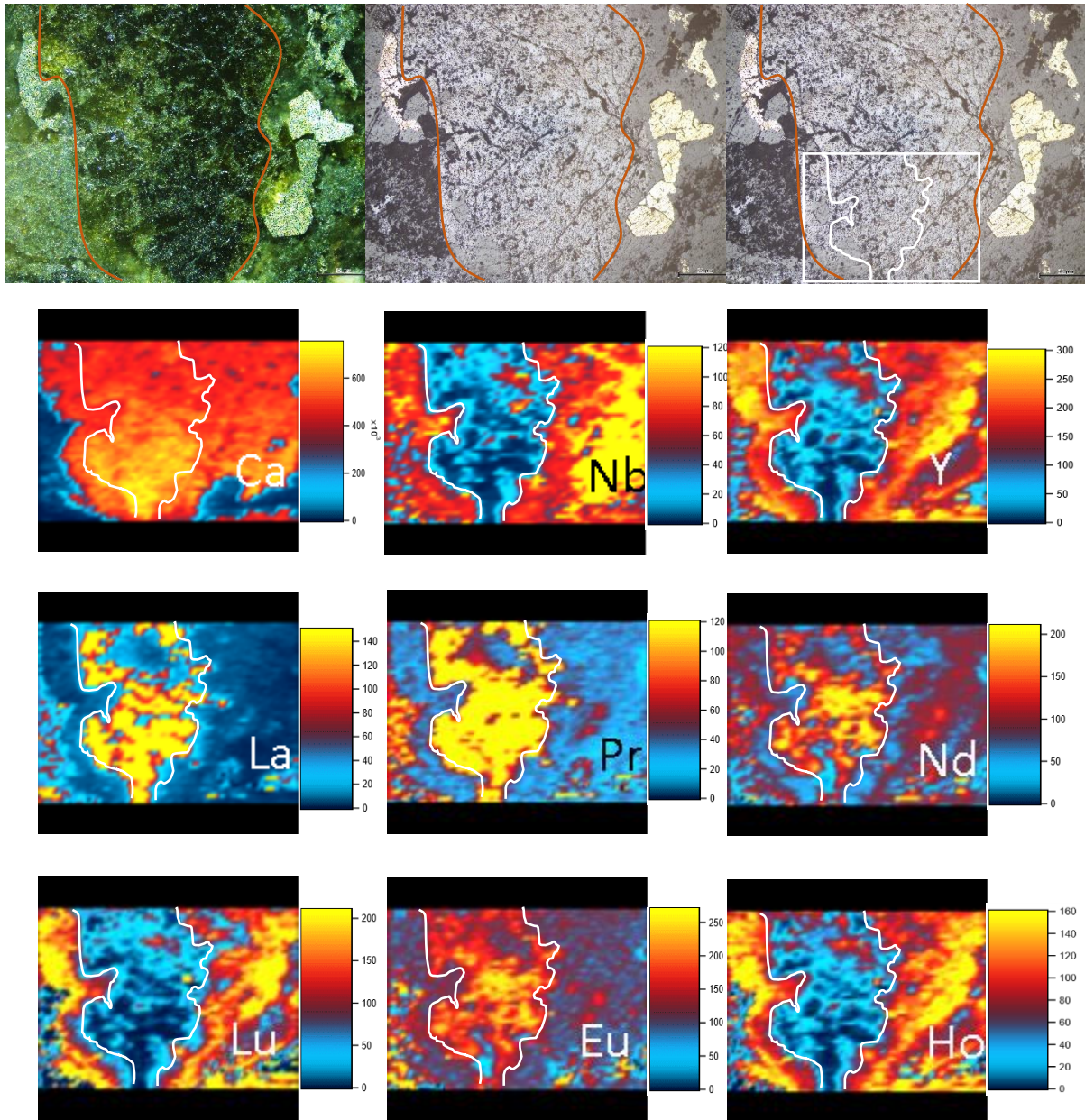
Figure 11: The first image is LA–ICP–MS element distribution map for garnet 89, which is located between the peak mineralisation and non-mineralised zone, so it represents the midway point of metal deposition. The first image is transmitted light, the second image is reflected light and the orange lines highlights the garnet grain. The third image is of the garnet grain, with the orange highlighting the grain boundary, and the white box showing the element map area and zonation of the elements displayed in the element maps below. Ca outlines the garnet, where the blue area is not garnet but quartz. Using this as a frame of reference, LREE are enriched in the core of the garnet, whereas HREE are enriched in the rim. Eu is also enriched in the core but is spread more evenly throughout the grain than the other REEs. Nb is also enriched in the rim, similar to garnet 87 but with a stark border between the rim and core. Concentrations are given in ppm. The relationship between rim and core is highlighted in white on the Nb element map.
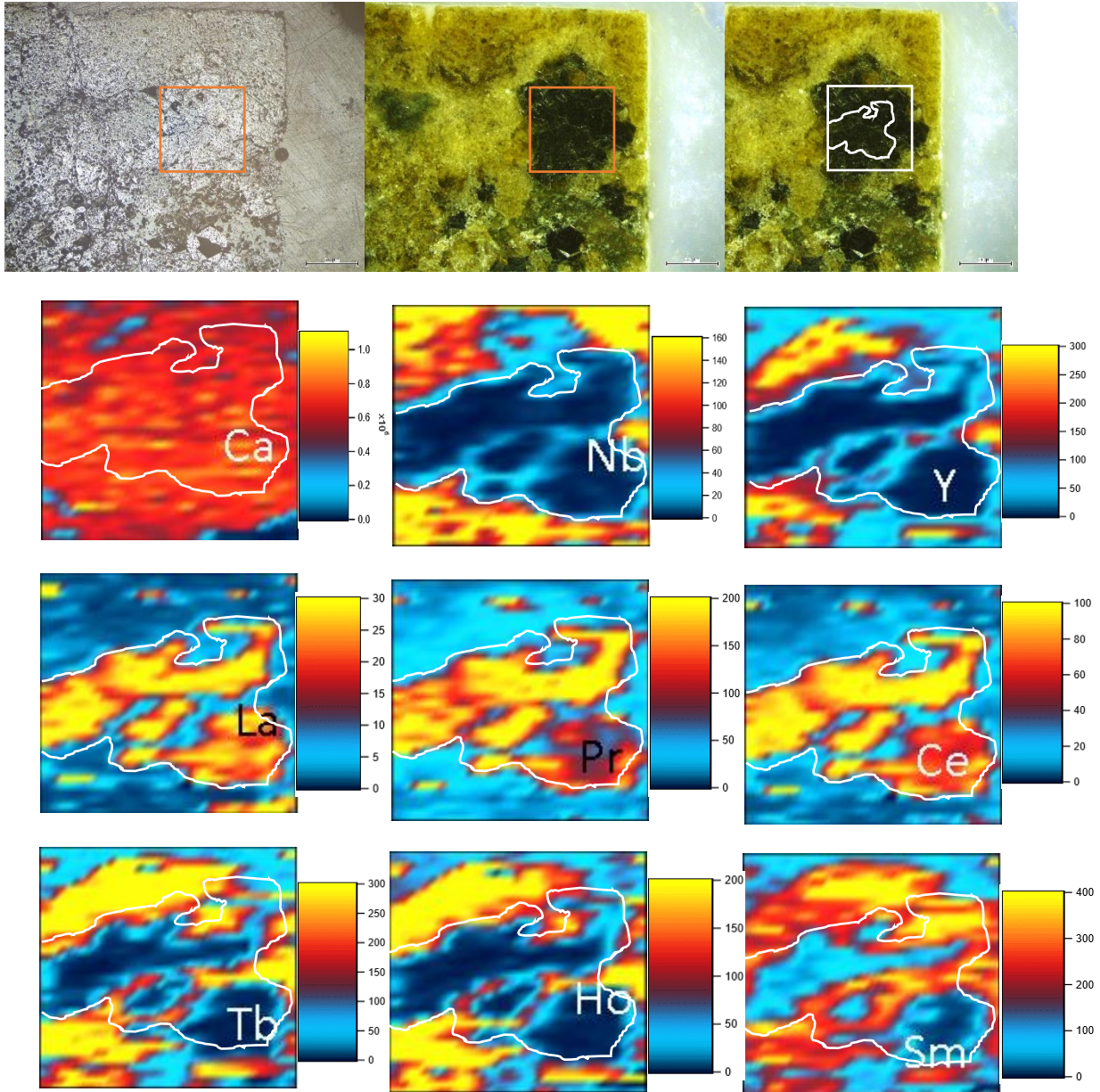
Figure 12: LA–ICP–MS element distribution map for garnet 91. The first image is reflected light, the second image is transmitted light and the orange lines highlights the garnet grain. The third image is of the garnet grain, with the orange highlighting the grain boundary, and the white box showing the element map area and zonation of the elements displayed in the element maps below. This garnet is located on the edge of the mineralised zone of the skarn, where it is approximately 25% enriched in Cu and Zn. Ca is used to highlight the shape of the grain, where the blue area is no longer garnet (potassium feldspar). LREE are enriched in the core, and HREE are enriched in the rim, with a nearly perfect mirror image of the concentrations. Nb is greater concentrated in the rim, even more so than garnet 89. Concentrations are given in ppm. The core vs. rim relationship, while weakly zoned, is highlighted in white on Nb element map.
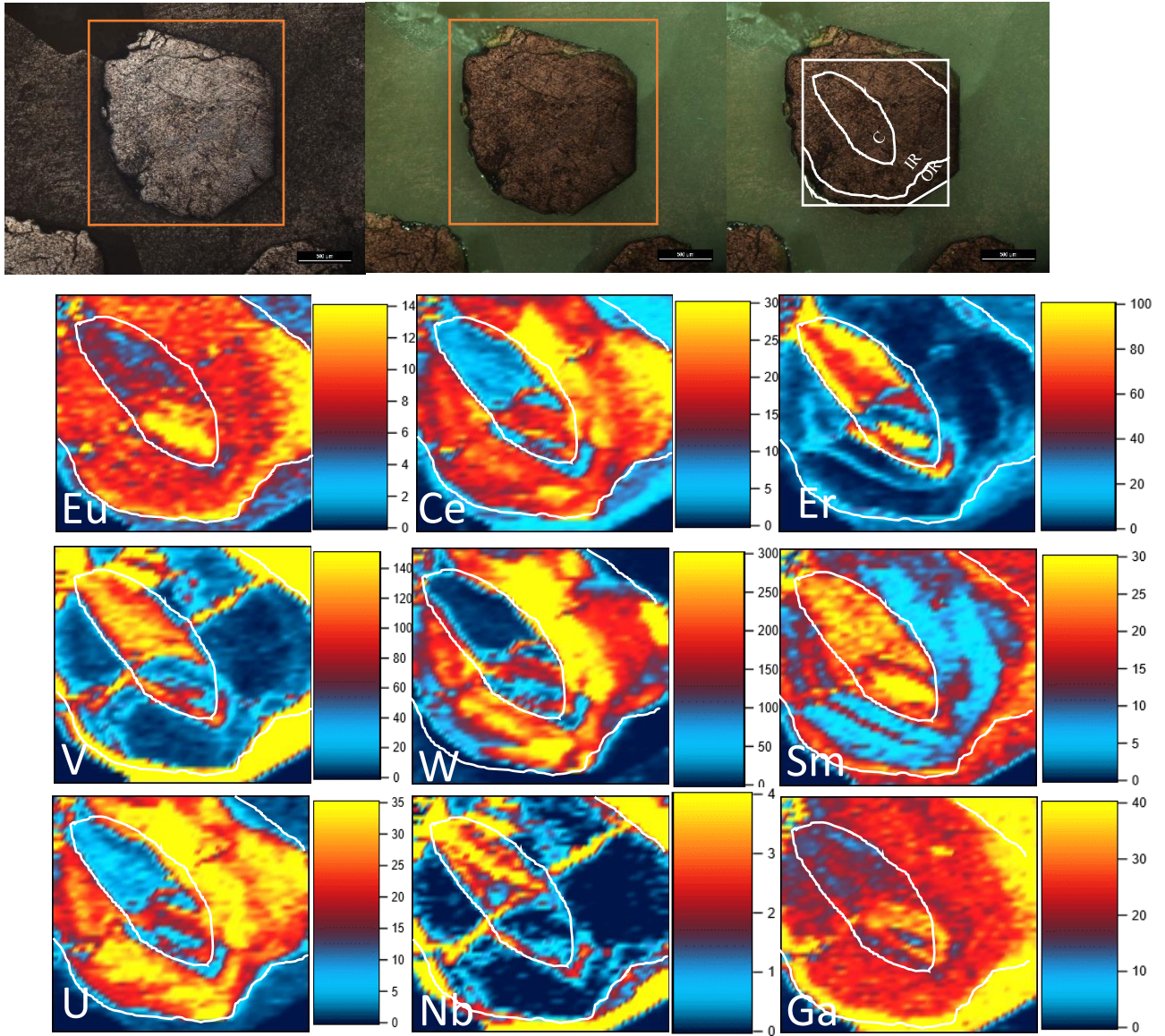
Figure 13: LA–ICP–MS element distribution map for garnet 83. This garnet is a type-I oscillatory zoned garnet within the mineralisation halo of the system. The first image is reflected light, the second image is transmitted light and the orange lines highlights the garnet grain within both. The third image is of the garnet grain, with the orange highlighting the grain boundary, and the white box showing the element map area and zonation of the elements displayed in the element maps below where C = core, IR = inner rim and OR = outer rim. LREE are enriched in the inner rim of the grain, and HREE are enriched in the core and rim. Incompatibles are preferentially uptaken by fractures in the grains and the outer rim, and form a secondary brief rim around the core of the grain.
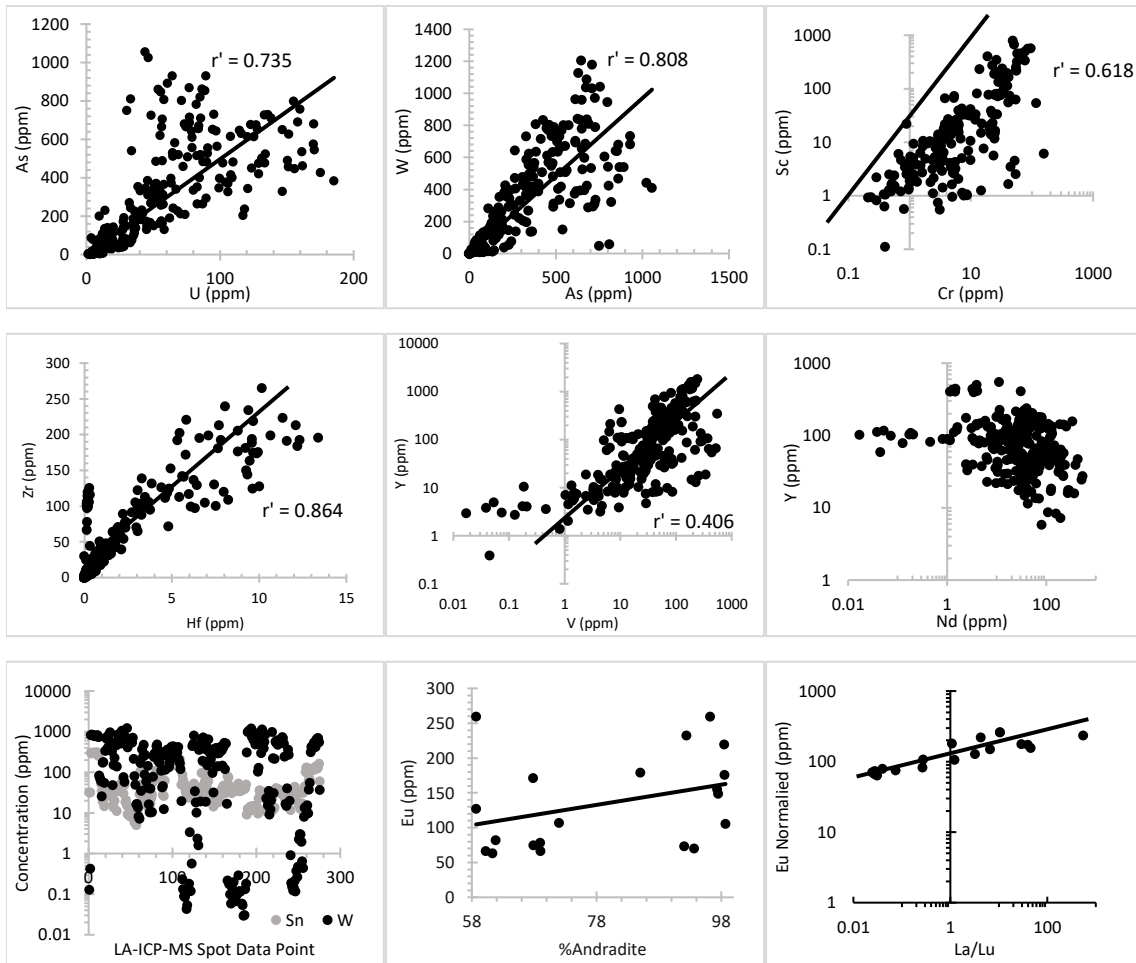
Figure 14: Relationships between elements from LA-ICP-MS spot data. The first seven plots are of all data points taken from every garnet. The last two plots are of averaged values of the transect across a garnet from each sample.

DISCUSSION

Incorporation of trace elements and substitution mechanisms in garnet

The general chemical formula for garnet is given as $X_3Y_2Z_3O_{12}$. X is defined as divalent

cations in eightfold coordination (Ca, Mg, Mn or Fe^{2+}), Y as trivalent cations in octahedral

coordination (Fe^{3+}, Al or Cr), and Z as quadrivalent cations in tetrahedral coordination

(almost exclusively Si) (Carlson *et al.,* 2006; Van Westernen *et al.,* 2000). Minor and trace

elements are substituted into this lattice depending on at least one of four main substitution

methods: occlusion, surface adsorption, interstitial solid solution and substitution

mechanisms (Bau, 1991; Rakovan & Reeder, 1996). Kinetic effects during mineral growth

effect the first two methods, while the last two are controlled by crystal chemistry. For REE

and Y to be incorporated into the garnet, they must be emplaced into the X^{2+} dodecahedral position, which is only balanced for Eu^{2+} ions (Carlson *et al.,* 2014). An imbalance in charge exists when the other REE+Ys are included, so altervalent substitution is required to balance the structure. Coupled substitution is commonly applied to account for this imbalance (e.g yttrium aluminium garnet-YAG substitution), where the change will be accounted for by another lower ionic charge element in either the X, Y or rarely the Z site. Often Na^+ will substitute into the X site (Smith, 2004). Structural vacancies can account for the change imbalance, though this is harder to evaluate.

Typically, zoned garnet is enriched in Y and HREE within the core (Otamendi *et al.,* 2002) due to their ability to resist re-equilibrium at elevated temperatures owing to their low intergranular and intragranular diffusivity (Bloch *et at.,* 2015). However, within this system almost all garnets exhibit the opposite; enrichment of LREE in the cores, and HREE within the rims. Inferences about the equilibrium partitioning of REE between bulk grossular–andradite (grandite) garnet can be made upon the basis of crystal chemistry and the substitution into the crystal lattice. The effective ionic radius of Ca^{2+} in the X site is comparative to that of Pr and Nd, which suggests purely on this basis that fluid partitioning in grandite garnets should be LREE–enriched with a peak at Pr (Nicolescu *et al.,* 1998). The lower concentrations of La and Ce may arise from the greater mismatch between these ionic radii and Ca, coupled with the tendency of La^{3+} to form complexes with Cl^- and F^- as oppose to Nd^{3+} and Sm^{3+} (Haas *et al.,* 1995). In hydrothermal fluid, REE transport is supported through chloride, fluoride and hydroxide complexes at various pH conditions (Migdisov, 2009). Skarn fluids typically contain substantial chloride complexes (Meinart, 2005) and fluorite is abundant throughout SAR8 have been identified as critical for transport of REE throughout deposits in Olympic Province (McPhie *et al.,* 2011). Fluorite ligands also enhance

HREE solubility, which could contribute to the high HREE concentrations observed (Haas, 1995).

A significant portion of the partitioning between HREE and LREE is likely due to YAG-type substitution discussed earlier, whereby Fe-rich and Al-rich zones are enriched in LREE and HREE via intracrystalline divalent substitution in the Y site (Smith *et al.*, 2004) (Gaspar *et al.*, 2008). However, the dominant REE+Y trends are from core to rim, whereby not all rims are Fe-rich and vice versa. It is likely of less importance than other mechanisms, instead contributing to divergence of general trends within each garnet. Magmatic hydrothermal fluids are typically LREE enriched and HREE depleted (Flynn and Wayne Burnham 1978).
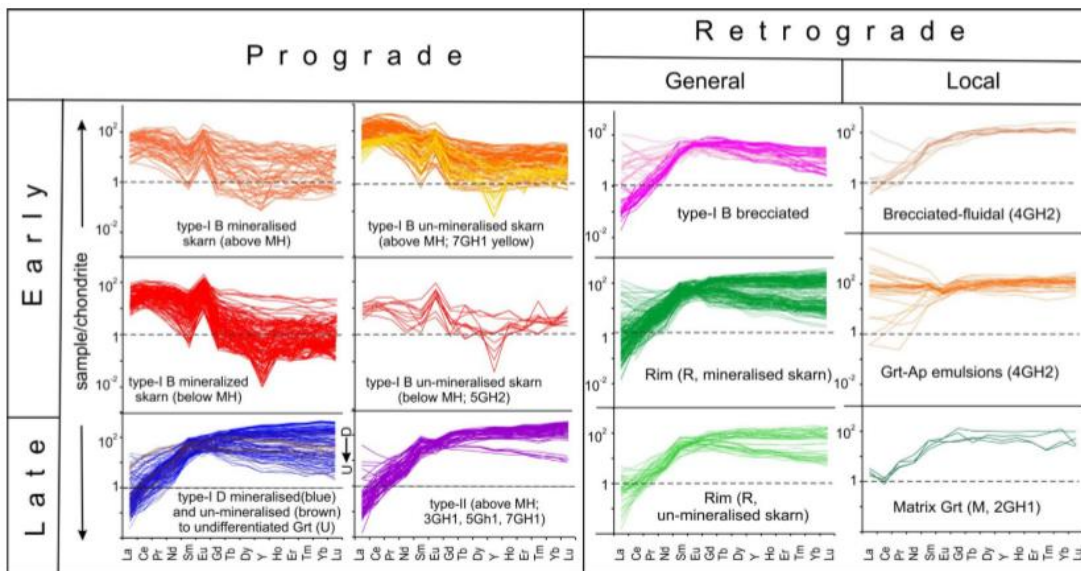
Figure 15: Chondrite–normalised (McDonough and Sun, 1995) REE+Y plots for garnets at Punt Hill (Nikolakopoulos, 2013).
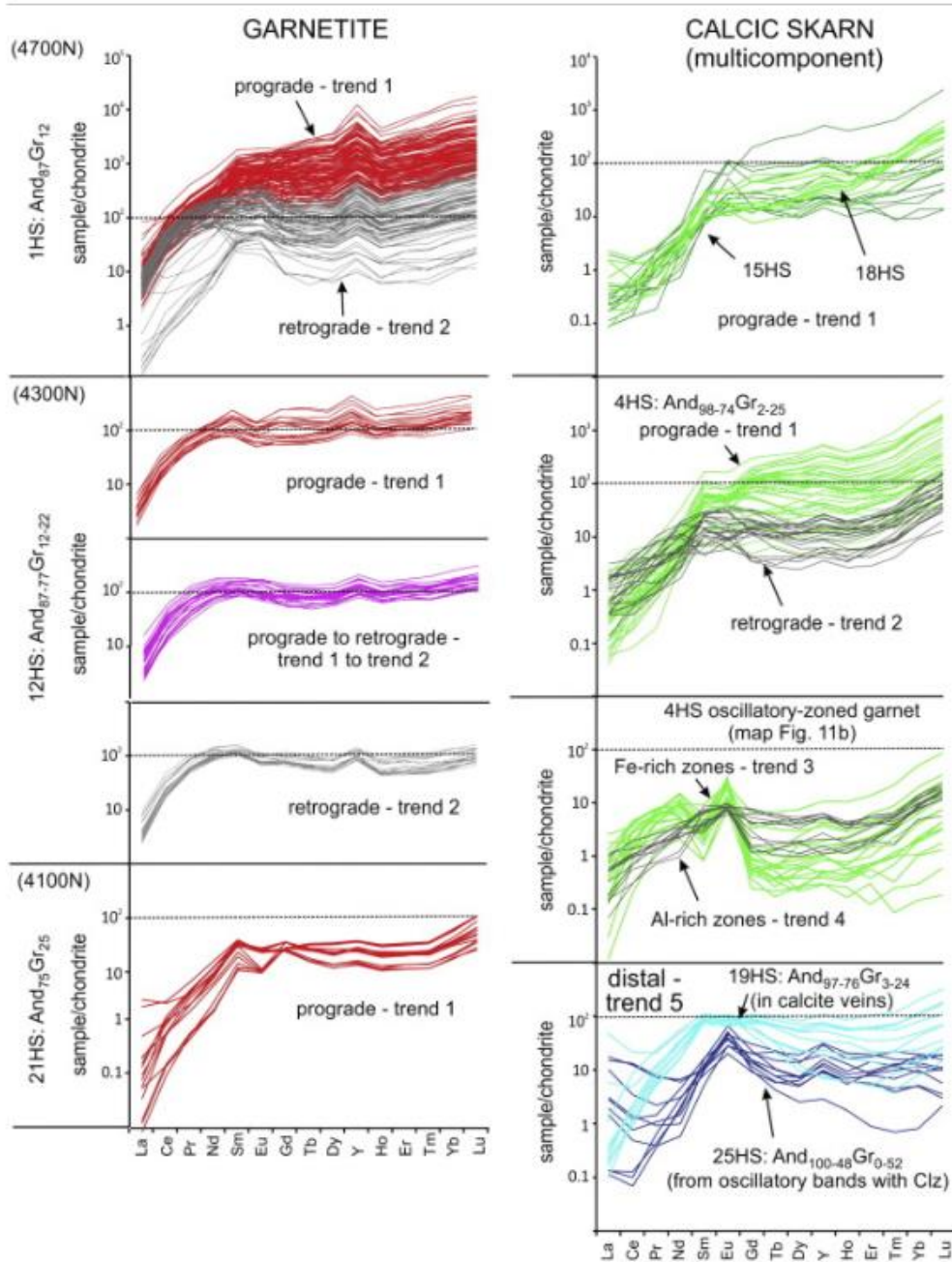
Figure 16: Chondrite–normalised (McDonough and Sun, 1995) REE+Y plots for garnet at Hillside (Ismail, 2014).

Developing an atlas style understanding of skarn mineralisation across the Eastern Gawler Craton

To develop an atlas like understanding of skarn systems in the Eastern Gawler Craton, the

studies conducted at Hillside (Ismail, 2014) and Punt Hill (Nikolakopoulos, 2013) were

chosen for their relationships to Pernatty Lagoon, distal and proximal respectively (Figure 1).

Both of the studies provide EMPA data, LA–ICP–MS spot data and element distribution

maps of garnet allowing for direct comparisons of data sets for prograde, retrograde and

garnet compositions to be assessed. Assessing these genetic similarities and differences has not been done and will allow for an assessment of whether these individual deposits are related on a systematic scale.

The distribution of REE+Y's in Pernatty Lagoon follow unique trends independent of garnet texture and instead differs greatest from prograde to retrograde stages. Prograde garnet is defined as a significant enrichment in LREE compared to HREE, with an enrichment in Eu relative to Sm. Retrograde garnet features a flat REE+Y distribution, with La and Ce depleted comparatively. Where La and Ce are depleted, Eu is depleted as well, with a Sm enrichment. Early prograde garnets at Punt Hill display similar trends to that at Pernatty Lagoon, with an, albeit smaller, depletion in HREE relative to LREE. The main difference is the La and Ce depletion, which is similar to that of the type-I D garnets (oscillatory zoned garnets, dark BSE image) and type-II garnets (weakly zoned inclusion rich garnets) (Figure 15). Most garnets in the Pernatty Lagoon prospect are inclusion rich and oscillatory zoned, indicating a mix of the styles of garnet at Punt Hill, which could account for a slight difference in observed trends. Punt Hill also displays Sm depletion and Eu enrichment for prograde garnet (Figure 17). Prograde Hillside garnets display a La, Ce depletion, but differ significantly in REE+Y distribution past this. LREE's are depleted relative to HREE's, similar to that of type-II Punt Hill garnets but unlike anything seen throughout Pernatty Lagoon.
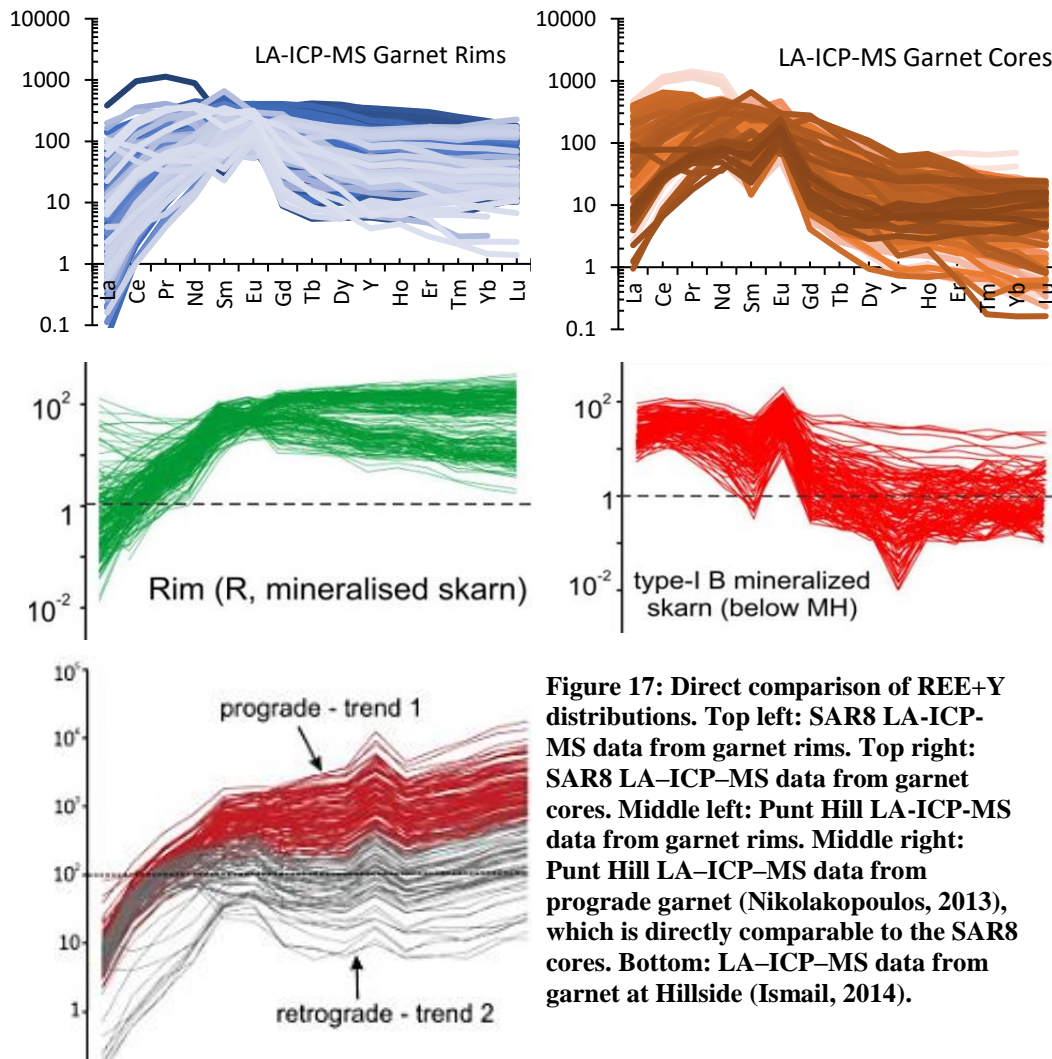
Figure 17: Direct comparison of REE+Y distributions. Top left: SAR8 LA-ICP-MS data from garnet rims. Top right: SAR8 LA–ICP–MS data from garnet cores. Middle left: Punt Hill LA-ICP-MS data from garnet rims. Middle right: Punt Hill LA–ICP–MS data from prograde garnet (Nikolakopoulos, 2013), which is directly comparable to the SAR8 cores. Bottom: LA–ICP–MS data from garnet at Hillside (Ismail, 2014).

Retrograde garnet in at Punt Hill and Hillside, compared to SAR8 garnet rims, are very similar in REE+Y distribution. All feature a depletion of LREE compared to HREE, with LREE being particularly low in La and Ce, and HREE distribution is flat. However, Punt Hill has no Eu anomaly, whereas Pernatty Lagoon has Eu depletion and Hillside has Eu enrichment only in Fe rich garnet. This strong decoupling of Eu from other REE in Fe-rich zoned garnet at Hillside relates only to a diffusion driven, closed system (Ismail, 2014; Smith, 2004). However, as seen in Figure 13, Pernatty Lagoon features a high correlation between La/Lu vs. Eu which reflects strongly on a Eu^{2+}/Eu^{3+} redox potential within the system, where $(La/Lu)_{cn}>1$ trends correlating with Eu indicates Eu occurs as Eu^{2+} and therefore acidic conditions for the sorption mechanics and a positive Eu anomaly (Smith,

2004; Gaspar, 2008). Where $(La/Lu)_{cn}<1$, it indicates a near-neutral to basic environment which extends the stability of Eu^{3+} (Bau, 1991). The lack of correlation in Eu between all the systems indicates that Eu is an independent, closed system process and doesn't reflect any potential for an atlas style representation of skarn systems throughout the Gawler Craton.

Both Hillside and Punt Hill contain a series of elements as potential mineralisation vectors. Hillside garnet is W-rich whereas Punt Hill is Sn-rich, which has been inferred to be related to variation in depth or the geotectonic context of magma during the Hiltaba magmatism (McPhie, 2011; Ehrig *et al.*, 2012; Nikolakopoulos, 2013). However, as seen in Figure 13, Sn and W in Pernatty Lagoon garnets while very enriched show no distinguishable trends as a function of depth, and W in particular is very sporadic in concentration. Sn and W both do not correlate with mineralisation, and so thereby make any assumptions of spatial relationship to fluid source very weak. Common across all three skarns is that no zonation trends exist based on major composition, major elements or trace elements. It is likely that host rock composition largely influences the fluid composition, disallowing for consistent zonation trends coupled with the likelihood that these patterns are potentially much larger scale than the Pernatty Lagoon/Punt Hill comparison, with Hillside being too greater distance away to observe a pattern. An additional study would be required to further determine the trend between all three deposits. Each deposit does however have an enrichment in W, Sn and As which indicates the fluid has a granitic affiliation, with a potential mafic component due to Cr enrichment, though this may just be influenced by the presence of rocks rich in this element along fluid pathways (Ehrig, 2012). Curiously, the Olympic Dam orebody is enriched in these same 'granitophile' elements (Verdugo *et al.*, 2017), but includes Mo which is depleted in Pernatty Lagoon and Punt Hill (Figure 8).

Eastern Gawler Craton skarns compared with other garnet skarns

Skarn garnets typically exhibit wide compositional variation at deposit and regional scale (Meinert 1992), but also change composition at grain scale via oscillatory, sector and growth zoning (Ciobanu & Cook 2004). However, this compositional variation allows for trends and correlations to be developed that can enable an understanding of discrete changes to the skarn system on a regional or local scale. Changes in fluid source, protolith type and fluid rock interactions have considerable effect on garnet geochemistry and can therefore allow for an understanding on the development of a skarn system (Smith 2004; Gaspar 2008; Ismail 2014). The Gawler Craton contains many widespread skarn systems, but the genetic similarities and differences are unknown.

Distinguishing the difference between Gawler Craton skarns and those of around the world is vital in developing a model to explain Gawler Craton skarn; not just that of skarn deposits in general. REE+Y distributions from garnet skarn in Beinn an Dubhaich Aureole, Skye, Scotland, UK (Smith, 2004) display LREE enrichment and flat, HREE distribution with a negative Eu anomaly. The main controls on this pattern is speculated to be from the equilibrium achieved between pyroxene, hydrothermal fluid and calcic garnet. Compositionally the garnets are within the same grandite range as Pernatty Lagoon. However, the ∑REE+Y is considerably less, and Fe-poor zones are enriched in HREE relative to LREE. Comparatively, garnets from Ocna de Fier, Romania show LREE enrichment and HREE depletion (Nicolescu, 1998). Typically, it is observed that more andradite rich garnets display LREE enrichment, whereas grossular rich are HREE enriched. Willsboro–Lewis wollastonite skarn garnets of the North–eastern Adirondack Mountains, New York, America (Whitney and Olmsted, 1998) describes the same andradite/grossular-rich REE distributions, leading to a dominant YAG-type substitution model to account for bulk REE patterns throughout worldwide skarn. However, these garnets have ∑REE+Y

magnitudes lower than that of Gawler Craton skarn. Moretti and Ottonello (1998) explored

the nature of YAG-REE fractionation in natural garnets to determine that it is only stable for

a limit of up to a few hundred ppm of bulk REE+Y. At greater concentrations, large

perturbations of crystal structure begin to induce polyhedral distortion, which alters the

nearest neighbour interactions to encourage further REE+Y substitution at any reasonable P–

T condition (Moretti and Ottonello, 1998). This further suggests the idea that YAG-type

substitution is not the dominate partitioning feature in Gawler Craton skarn, with X site Ca^{2+}

substitution and the degree of effective ionic radius matching. The Buckhorn Mountain

(Crown Jewel) gold skarn deposit, Okanogan Country, Washington (Gaspar, 2008) presents a

trace element distribution similar to Pernatty Lagoon, with extremely depleted large ion

lithophile elements (LILE).

By evaluating these contrasts, a unique model to Gawler Craton skarns can be developed.

Marked enrichment in W, Sn, As, U and Cr within garnet is exclusive to GC skarn, with high

∑REE+Y. Andradite–grossular garnet compositions are common throughout skarn garnet

systems across the world, and these compositions have largely played a role on distribution of

REE within garnet due to YAG-style fractionation, but Gawler Craton skarns are so enriched

with REE+Y that this fractionation is only a secondary factor in the REE+Y distribution;

forcing alternative substitution methods mentioned earlier to be more dominate. The

significant depletion of La and Ce relative to other LREE, especially within garnet rims, is

rarely seen elsewhere but the Gawler Craton skarns, and creates a unique REE+Y distribution

when coupled with low HREE enrichment compared to LREE within the cores of garnets,

and low LREE enrichment compared to HREE within the rims. The culmination of these

features indicates the composition of the fluid source and the interactions between host

rock/fluid within the Gawler Craton are not seen anywhere else in the world.

CONCLUSIONS

- Geochemical signatures from Punt Hill, Hillside and Pernatty Lagoon suggest the skarn systems are linked through a broad, regional style development due to their similar REE+Y distribution and ∑REE+Y. However, significant differences are present due to fluid–rock interactions involving different fluid sources at each location. Eastern Gawler Craton skarn systems are therefore definable on a broad scale comparatively to skarns of the world, but closed-system interactions have significant independent influences.

- Eu is fractionated differently to the REE+Y trend as it is present as either Eu^{2+} or Eu^{3+} as a function of the redox conditions present.

- YAG-style REE+Y fractionation only partly accounts for the distribution of REE+Y patterns. X-site ionic radii substitution accounts for the unusual LILE fractionation, with Cl^- and F^- complexes being a major suppository of La^{3+} within hydrothermal fluids. This differentiates South Australian skarns from worldwide skarns via the high ∑REE+Y forcing alternative substitution methods than YAG-style between grossular/andradite compositions.

- Marked enrichment in W, Sn, As and Cr across all three deposits, while initially thought to be a vector for mineralisation and fluid flow, is inconclusive. The enrichment is likely due to host rock compositions and rocks associated with the fluid pathways. The skarn deposits are linked by these enrichments though, coupled with the high ∑REE+Y and U, similar garnet compositions ($And_{99-85}Gr_{0-13}Sp_{1-2} - And_{74-56}Gr_{23-41}Sp_{1-2}$), and a unique REE+Y distribution; they form a unique skarn deposit unlike other skarns across the world with differences between the three due to independent closed system interactions.

ACKNOWLEGMENTS

Firstly, I would like to thank Nestorek Wyra whom worked on the sister project to mine; studying the isotopic characterisation of the mineralised skarn in Pernatty Lagoon. Your assistance, motivation and constant support has been incredible. Secondly, Ben Wade and Sarah Gilbert from Adelaide Microscopy, I cannot thank you enough, your advice, patience and support was unbelievable. A big thanks to Alec Walsh for his guidance and support throughout the year. Everyone at the Department of State Developments drill core library for being exceptionally accommodating and cooperative throughout the year.

And lastly to my supervisor Martin Hand; without whom this project would never have been possible.

REFERENCES

Allen, S. R., Simpson, C. J., McPhie, J., & Daly, S. J. (2003). Stratigraphy, distribution and geochemistry of widespread felsic volcanic units in the Mesoproterozoic Gawler Range Volcanics, South Australia. *Australian Journal of Earth Sciences, 50*(1), 97-112. doi:10.1046/j.1440-0952.2003.00980.x

Bastrakov, E. N., Skirrow, R. G., & Davidson, G. J. (2007). Fluid evolution and origins of iron oxide Cu-Au prospects in the Olympic Dam district, Gawler Craton, South Australia. *Economic Geology, 102*(8), 1415-1440.

Bau, M. (1991). Rare-earth element mobility during hydrothermal and metamorphic fluid-rock interaction and the significance of the oxidation state of europium. *Chemical Geology, 93*(3-4), 219-230.

Bau, M., & Dulski, P. (1995). Comparative study of yttrium and rare-earth element behaviours in fluorine-rich hydrothermal fluids. *Contributions to Mineralogy and Petrology, 119*(2), 213-223. doi:10.1007/bf00307282

Belperio, A., Flint, R., & Freeman, H. (2007). Prominent Hill: A hematite-dominated, iron oxide copper-gold system. *Economic Geology, 102*(8), 1499-1510.

Bloch, E., Ganguly, J., Hervig, R., & Cheng, W. (2015). 176Lu–176Hf geochronology of garnet I: experimental determination of the diffusion kinetics of Lu3+ and Hf4+ in garnet, closure temperatures and geochronological implications. *Contributions to Mineralogy and Petrology, 169*(2), 12. doi:10.1007/s00410-015-1109-8

Bowden, B., Fraser, G., Davidson, G. J., Meffre, S., Skirrow, R., Bull, S., & Thompson, J. (2016). Age constraints on the hydrothermal history of the Prominent Hill iron oxide copper-gold deposit, South Australia. *Mineralium Deposita*, 1-19.

Brugger, J., Lahaye, Y., Costa, S., Lambert, D., & Bateman, R. (2000). Inhomogeneous distribution of REE in scheelite and dynamics of Archaean hydrothermal systems (Mt. Charlotte and Drysdale gold deposits, Western Australia). *Contributions to Mineralogy and Petrology, 139*(3), 251-264. doi:10.1007/s004100000135

Carlson, W. D. (2006). Rates of Fe, Mg, Mn, and Ca diffusion in garnet. *American Mineralogist, 91*(1), 1-11. doi:10.2138/am.2006.2043

Carlson, W. D. (2012). Rates and mechanism of Y, REE, and Cr diffusion in garnet. *American Mineralogist, 97*(10), 1598-1618. doi:10.2138/am.2012.4108

Carlson William, D., Gale Julian, D., & Wright, K. (2014). Incorporation of Y and REEs in aluminosilicate garnet: Energetics from atomistic simulation *American Mineralogist* (Vol. 99, pp. 1022).

Ciobanu, C. L., Wade, B. P., Cook, N. J., Mumm, A. S., & Giles, D. (2013). Uranium-bearing hematite from the Olympic Dam Cu–U–Au deposit, South Australia: A geochemical tracer and reconnaissance Pb–Pb geochronometer. *Precambrian Research, 238*, 129-147.

Conor, C., Raymond, O., Baker, T., Teale, G., Say, P., & Lowe, G. (2010). *Alteration and mineralisation in the Moonta-Wallaroo Cu-Au mining field region, Olympic Domain, South Australia* (Vol. 3).

Davidson, G. J., Paterson, H., Meffre, S., & Berry, R. F. (2007). Characteristics and origin of the oak dam East Breccia-hosted, iron oxide Cu-U-(Au) deposit: Olympic Dam region, Gawler Craton, South Australia. *Economic Geology, 102*(8), 1471-1498.

Ducoux, M., Branquet, Y., Jolivet, L., Arbaret, L., Grasemann, B., Rabillard, A., . . . Drufin, S. (2017). Synkinematic skarns and fluid drainage along detachments: The West Cycladic Detachment System on Serifos Island (Cyclades, Greece) and its related mineralization. *Tectonophysics, 695*, 1-26. doi:https://doi.org/10.1016/j.tecto.2016.12.008

Ehrig, K., McPhie, J., & Kamenetsky, V. (2012). *Geology and mineralogical zonation of the Olympic Dam iron oxide Cu-U-Au-Ag deposit, South Australia* (Vol. 16).

Fabris, A., Katona, L., Reed, G., Keeping, T., Gordon, G., Gouthas, G., & Swain, G. (2016). *Mapping the Punt Hill IOCG system using geophysical, geochemical and spectral methods–an integrated approach.* Paper presented at the ASEG Extended Abstracts 2016: 25th International Geophysical Conference and Exhibition.

Flynn, R. T., & Wayne Burnham, C. (1978). An experimental determination of rare earth partition coefficients between a chloride containing vapor phase and silicate melts. *Geochimica et Cosmochimica Acta, 42*(6), 685-701. doi:https://doi.org/10.1016/0016-7037(78)90087-X

Gaspar, M., Knaack, C., Meinert, L. D., & Moretti, R. (2008). REE in skarn systems: A LA-ICP-MS study of garnets from the Crown Jewel gold deposit. *Geochimica et Cosmochimica Acta, 72*(1), 185-205. doi:https://doi.org/10.1016/j.gca.2007.09.033

Haas, J. R., Shock, E. L., & Sassani, D. C. (1995). Rare earth elements in hydrothermal systems: Estimates of standard partial molal thermodynamic properties of aqueous complexes of the rare earth elements at high pressures and temperatures. *Geochimica et Cosmochimica Acta, 59*(21), 4329-4350. doi:https://doi.org/10.1016/0016-7037(95)00314-P

Hand, M., Reid, A., & Jagodzinski, L. (2007). Tectonic framework and evolution of the Gawler craton, southern Australia. *Economic Geology, 102*(8), 1377-1395.

Ismail, R., Ciobanu, C. L., Cook, N. J., Teale, G. S., Giles, D., Mumm, A. S., & Wade, B. (2014). Rare earths and other trace elements in minerals from skarn assemblages, Hillside iron oxide–copper–gold deposit, Yorke Peninsula, South Australia. *Lithos, 184*, 456-477. doi:http://dx.doi.org/10.1016/j.lithos.2013.07.023

Ismail, R., Ciobanu, C. L., Cook, N. J., Teale, G. S., Giles, D., Mumm, A. S., & Wade, B. (2014). Rare earths and other trace elements in minerals from skarn assemblages, Hillside iron oxide–copper–gold deposit, Yorke Peninsula, South Australia. *Lithos, 184*, 456-477.

Jochum, K. P., Weis, U., Stoll, B., Kuzmin, D., Yang, Q., Raczek, I., . . . Enzweiler, J. (2011). Determination of Reference Values for NIST SRM 610–617 Glasses Following ISO Guidelines. *Geostandards and Geoanalytical Research, 35*(4), 397-429. doi:10.1111/j.1751-908X.2011.00120.x

Jochum, K. P., Willbold, M., Raczek, I., Stoll, B., & Herwig, K. (2005). Chemical Characterisation of the USGS Reference Glasses GSA-1G, GSC-1G, GSD-1G, GSE-1G, BCR-2G, BHVO-2G and BIR-1G Using EPMA, ID-TIMS, ID-ICP-MS and LA-ICP-MS. *Geostandards and Geoanalytical Research, 29*(3), 285-302. doi:10.1111/j.1751-908X.2005.tb00901.x

Kawabe, I. (1992). Lanthanide tetrad effect in the Ln3+ ionic radii and refined spin-pairing energy theory. *Geochemical Journal, 26*(6), 309-335.

Kontonikas-Charos, A., Ciobanu, C. L., & Cook, N. J. (2014). Albitization and redistribution of REE and Y in IOCG systems: Insights from Moonta-Wallaroo, Yorke Peninsula, South Australia. *Lithos, 208*, 178-201. doi:http://dx.doi.org/10.1016/j.lithos.2014.09.001

Lane, K., Jagodzinski, E. A., Dutch, R., Reid, A. J., & Hand, M. (2015). Age constraints on the timing of iron ore mineralisation in the southeastern Gawler Craton. *Australian Journal of Earth Sciences, 62*(1), 55-75. doi:10.1080/08120099.2015.993160

McDonough, W. F., & Sun, S. s. (1995). The composition of the Earth. *Chemical Geology, 120*(3), 223-253. doi:http://dx.doi.org/10.1016/0009-2541(94)00140-4

McIntire, W. L. (1963). Trace element partition coefficients—a review of theory and applications to geology. *Geochimica et Cosmochimica Acta, 27*(12), 1209-1264. doi:http://dx.doi.org/10.1016/0016-7037(63)90049-8

McPhie, J., Kamenetsky, V., Allen, S., Ehrig, K., Agangi, A., & Bath, A. (2011). The fluorine link between a supergiant ore deposit and a silicic large igneous province. *Geology, 39*(11), 1003-1006. doi:10.1130/G32205.1

Migdisov, A. A., Williams-Jones, A. E., & Wagner, T. (2009). An experimental study of the solubility and speciation of the Rare Earth Elements (III) in fluoride- and chloride-bearing aqueous solutions at temperatures up to 300°C. *Geochimica et Cosmochimica Acta, 73*(23), 7087-7109. doi:https://doi.org/10.1016/j.gca.2009.08.023

Morrissey, L. J., Hand, M., Lane, K., Kelsey, D. E., & Dutch, R. A. (2016). Upgrading iron-ore deposits by melt loss during granulite facies metamorphism. *Ore Geology Reviews, 74*(Supplement C), 101-121. doi:https://doi.org/10.1016/j.oregeorev.2015.11.012

Morrow, N., & McPhie, J. (2000). Mingled silicic lavas in the Mesoproterozoic Gawler Range Volcanics, South Australia. *Journal of Volcanology and Geothermal Research, 96*(1), 1-13. doi:https://doi.org/10.1016/S0377-0273(99)00143-2

Nicolescu, S., Cornell, D. H., Sodervall, U., & Odelius, H. (1998). Secondary ion mass spectrometry analysis of rare earth elements in grandite garnet and other skarn related silicates. *European Journal of Mineralogy, 10*(2), 251-259.

Otamendi, J. E., de la Rosa, J. s. D., Douce, A. E. P. o., & Castro, A. (2002). Rayleigh fractionation of heavy rare earths and yttrium during metamorphic garnet growth. *Geology, 30*(2), 159-162. doi:10.1130/0091-7613(2002)030<0159:RFOHRE>2.0.CO;2

Payne, J. L., Barovich, K. M., & Hand, M. (2006). Provenance of metasedimentary rocks in the northern Gawler Craton, Australia: Implications for Palaeoproterozoic reconstructions. *Precambrian Research, 148*(3), 275-291. doi:https://doi.org/10.1016/j.precamres.2006.05.002

Payne, J. L., Hand, M., Barovich, K. M., & Wade, B. P. (2008). Temporal constraints on the timing of high-grade metamorphism in the northern Gawler Craton: implications for assembly of the Australian Proterozoic. *Australian Journal of Earth Sciences, 55*(5), 623-640. doi:10.1080/08120090801982595

Peng, H.-J., Zhang, C.-q., Mao, J.-w., Santosh, M., Zhou, Y.-m., & Hou, L. (2015). Garnets in porphyry–skarn systems: A LA–ICP–MS, fluid inclusion, and stable isotope study of garnets from the Hongniu–Hongshan copper deposit, Zhongdian area, NW Yunnan Province, China. *Journal of Asian Earth Sciences, 103*, 229-251.

Raimondo, T., Payne, J., Wade, B., Lanari, P., Clark, C., & Hand, M. (2017). Trace element mapping by LA-ICP-MS: assessing geochemical mobility in garnet. *Contributions to Mineralogy and Petrology, 172*(4), 17. doi:10.1007/s00410-017-1339-z

RAKOVAN, J., & REEDER, R. J. (1996). Intracrystalline rare earth element distributions in apatite: Surface structural influences on incorporation during growth. *Geochimica et Cosmochimica Acta, 60*(22), 4435-4445. doi:https://doi.org/10.1016/S0016-7037(96)00244-X

REID, A., FLINT, R., MAAS, R., HOWARD, K., & BELOUSOVA, E. (2009). Geochronological and isotopic constraints on Palaeoproterozoic skarn base metal mineralisation in the central Gawler Craton, South Australia. *Ore Geology Reviews, 36*(4), 350-362.

REID, A., JOURDAN, F., & JAGODZINSKI, E. (2017). Mesoproterozoic fluid events affecting Archean crust in the northern Olympic Cu–Au Province, Gawler Craton: insights from 40Ar/39Ar thermochronology. *Australian Journal of Earth Sciences*, 1-17.

REID, A., SMITH, R. N., BAKER, T., JAGODZINSKI, E. A., SELBY, D., GREGORY, C. J., & SKIRROW, R. G. (2013). Re-Os dating of molybdenite within hematite breccias from the Vulcan Cu-Au prospect, Olympic Cu-Au province, South Australia. *Economic Geology, 108*(4), 883-894.

REID, A. J., & FABRIS, A. (2015). Influence of preexisting low metamorphic grade sedimentary successions on the distribution of iron oxide copper-gold mineralization in the Olympic Cu-Au province, Gawler craton. *Economic Geology, 110*(8), 2147-2157.

REID, A. J., SWAIN, G., MASON, D., & MAAS, R. (2011). Nature and timing of Cu-Au-Zn-Pb mineralisation at Punt Hill, eastern Gawler Craton. *MESA Journal, 60*, 7-17.

SCHLEGEL, T. U., & HEINRICH, C. A. (2015). Lithology and hydrothermal alteration control the distribution of copper grade in the Prominent Hill iron oxide-copper-gold deposit (Gawler craton, South Australia). *Economic Geology, 110*(8), 1953-1994.

SCHLEGEL, T. U., WAGNER, T., BOYCE, A., & HEINRICH, C. A. (2016). A magmatic source of hydrothermal sulfur for the Prominent Hill deposit and associated prospects in the Olympic iron oxide copper-gold (IOCG) province of South Australia. *Ore Geology Reviews*.

SKIRROW, R. G., BASTRAKOV, E. N., BAROVICH, K., FRASER, G. L., CREASER, R. A., FANNING, C. M., . . . DAVIDSON, G. J. (2007). Timing of iron oxide Cu-Au-(U) hydrothermal activity and Nd isotope constraints on metal sources in the Gawler craton, South Australia. *Economic Geology, 102*(8), 1441-1470.

SKIRROW, R. G., & DAVIDSON, G. J. (2007). A special issue devoted to Proterozoic iron oxide Cu-Au-(U) and gold mineral systems of the Gawler Craton: preface. *Economic Geology, 102*(8), 1373-1375.

SMITH, M. P., HENDERSON, P., JEFFRIES, T. E. R., LONG, J., & WILLIAMS, C. T. (2004). The Rare Earth Elements and Uranium in Garnets from the Beinn an Dubhaich Aureole, Skye, Scotland, UK: Constraints on Processes in a Dynamic Hydrothermal System. *Journal of Petrology, 45*(3), 457-484. doi:10.1093/petrology/egg087

SWAIN, G., WOODHOUSE, A., HAND, M., BAROVICH, K., SCHWARZ, M., & FANNING, C. M. (2005). Provenance and tectonic development of the late Archaean Gawler Craton, Australia; U–Pb zircon, geochemical and Sm–Nd isotopic implications. *Precambrian Research, 141*(3–4), 106-136. doi:https://doi.org/10.1016/j.precamres.2005.08.004

VAN WESTRENEN, W., ALLAN, N. L., BLUNDY, J. D., PURTON, J. A., & WOOD, B. J. (2000). Atomistic simulation of trace element incorporation into garnets—comparison with experimental garnet-melt partitioning data. *Geochimica et Cosmochimica Acta, 64*(9), 1629-1639. doi:https://doi.org/10.1016/S0016-7037(00)00336-7

VERDUGO IHL, M., CIOBANU, C., COOK, N., COURTNEY-DAVIES, L., EHRIG, K., & GILBERT, S. (2017). *Trace element signatures in U-W-Sn-Mo zoned hematite from the IOCG deposit at Olympic Dam, South Australia*.

WHITNEY, P. R., & OLMSTED, J. F. (1998). Rare earth element metasomatism in hydrothermal systems: the Willsboro-Lewis wollastonite ores, New York, USA. *Geochimica et Cosmochimica Acta, 62*(17), 2965-2977. doi:https://doi.org/10.1016/S0016-7037(98)00230-0

WOODHEAD, J. D., HELLSTROM, J., HERGT, J. M., GREIG, A., & MAAS, R. (2007). Isotopic and Elemental Imaging of Geological Materials by Laser Ablation Inductively Coupled Plasma-Mass Spectrometry. *Geostandards and Geoanalytical Research, 31*(4), 331-343. doi:10.1111/j.1751-908X.2007.00104.x

APPENDIX A

Electron Microprobe Analysis

Quantitative major and minor element compositional data was generated for 25 areas across

14 samples. The EMPA used was a Cameca SX–5 electron probe microanalyzer (Adelaide

Microscopy, South Australia). Accelerating voltage was 20kV and a beam current of 20nA.

Table 3: EMPA standards, X–ray lines, typical minimum detection limits and count times.

Element	Standard	X-ray line	Count time (s) unknown/background	Average mdl (ppm)
Na	Albite	Na Kα	20/10	120
K	Sanadine	K Kα	20/10	130
Ca	Wollastonite	Ca Kα	20/10	120
Mn	Rhodonite	Mn Kα	20/10	300
Mg	Almandine	Mg Kα	20/10	220
Fe	Almandine	Fe Kα	20/10	350
Al	Almandine	Al Kα	20/10	250
Si	Almandine	Si Kα	20/10	300
Cr	Chromite	Cr Kα	20/10	400
Ti	Rutile	Ti Kα	20/10	150
F	Synthetic CaF$_2$	F Kα	30/15	300
Cl	Tugtupite	Cl Kα	30/15	200
P	Apatite	P Kα	20/10	200
S	Marcasite	S Kα	30/15	170
As	GaAs	As Lα	20/10	600
Nb	Nb metal	Nb Lα	20/10	360
V	V metal	V Lα	20/10	400
Sr	Celestite	Sr Lα	20/10	600
Sc	Sc metal	Sc Kα	20/10	180
Zr	Synthetic zircon	Zr Lα	20/10	325
Hf	Zircon	Hf Lα	20/10	740
Ta	Ta metal	Ta Lα	20/10	1025
W	W metal	W Lα	20/10	750
Pb	Synthetic Pb-silicate	Pb Mß	20/10	375
Th	Huttonite	Th Mα	20/10	1500
U	UO$_2$	U Mß	20/10	360

Table 4: Electron microprobe analyse of garnet samples in SAR8.

	65 Core/Light	65 Rim/Dark	77 Core/Light	77 Rim/Dark	78 Core/Light	78 Rim/Dark
CaO	32.20	32.60	32.25	33.79	32.72	33.89
MgO	0.03	0.05	0.02	0.02	0.08	0.08
TiO2	0.09	1.09		0.05		0.30
SiO2	35.61	36.40	34.76	36.08	35.17	35.49
Al2O3	1.41	5.53		9.32	0.04	8.64
Fe2O3	29.42	22.08	31.31	19.35	30.61	19.08
MnO	0.48	0.64	0.55	0.77	0.40	0.74
Cr2O3		0.05				
Cl	0.02	0.02				
F	0.22	0.10	0.09	0.62		0.80
K2O	0.06	0.10				
P2O5	0.05	0.05	0.03	0.03	0.03	0.03
Na2O	0.07	0.11				
BaO						
V2O3		0.10		0.05		0.04
ZnO		0.07				
TOTAL	**99.57**	**98.94**	**99.04**	**99.87**	**99.13**	**98.79**
Formulae						
$(Ca,Mg,Mn)_6(Fe,Al)_4Si_6O_{24}$						
Mg	0.009	0.013	0.005	0.005	0.017	0.018
Mn	0.069	0.089	0.074	0.102	0.051	0.098
Ca	5.963	5.915	6.011	5.750	5.874	5.771
Total	**6.041**	**6.017**	**6.09**	**5.857**	**5.942**	**5.887**
Fe	3.845	2.798	4.162	2.417	3.911	2.325
Al	0.326	1.265		1.879	0.008	1.368
Ti	0.012	0.129		0.007		0.036
Cr		0.005				
Total	**4.183**	**4.197**	**4.162**	**4.303**	**3.919**	**3.729**
Si	5.878	5.940	5.973	5.928	5.913	5.888
Al	0.122	0.06	0.027	0.072	0.087	0.112
Total	**6.000**	**6.000**	**6.000**	**6.000**	**6.000**	**6.000**
Total	*16.224*	*16.214*	*16.252*	*16.16*	*15.861*	*15.616*
Spessartine	1.1	1.5	1.4	1.8	1.0	1.8
Grossular	6.4	26.4	0.1	39.5	0.5	38.0
Andradite	92.5	72.0	98.5	58.7	98.5	60.2

	79 Light	83 Light	83 Dark	84 Core	84 Rim	85 Core/Dark
CaO	33.84	32.42	32.55	33.11	32.41	32.36
MgO		0.06	0.02	0.04		0.07
TiO2	0.41	0.02	0.21	0.70	0.29	
SiO2	35.12	35.41	36.97	35.77	35.54	34.44
Al2O3	8.90		5.28	6.94	6.95	0.30
Fe2O3	18.99	31.06	24.04	21.91	22.22	29.74
MnO	0.69	0.35	0.69	0.70	0.86	0.40
Cr2O3						
Cl					0.03	
F	0.88		0.07	0.15	0.20	0.13
K2O			0.03		0.03	
P2O5	0.04		0.03	0.03	0.06	0.03
Na2O				0.05	0.09	
BaO					0.03	
V2O3						
ZnO						0.07
TOTAL	**98.57**	**99.42**	**99.93**	**99.42**	**98.66**	**97.49**

Formulae
(Ca,Mg,Mn)$_6$(Fe,Al)$_4$Si$_6$O$_{24}$

	79 Light	83 Light	83 Dark	84 Core	84 Rim	85 Core/Dark
Mg	0.000	0.014	0.005	0.011	0.000	0.015
Mn	0.092	0.045	0.092	0.094	0.128	0.052
Ca	6.012	5.895	5.799	5.965	5.900	5.963
Total	**6.104**	**5.954**	**5.896**	**6.070**	**6.028**	**6.030**
Fe	2.311	4.019	3.154	2.756	2.806	3.888
Al	1.510		1.165	1.399	1.436	0.021
Ti	0.052	0.003	0.025	0.085	0.038	
Cr						
Total	**3.873**	**4.022**	**4.344**	**4.24**	**4.28**	**3.909**
Si	5.945	5.986	5.896	5.882	5.890	5.959
Al	0.055	0.014	0.104	0.118	0.11	0.041
Total	**6.000**	**6.000**	**6.000**	**6.000**	**6.000**	**6.000**
Total	*15.977*	*15.976*	*16.24*	*16.31*	*16.308*	*15.939*
Spessartine	1.7	0.8	1.6	1.6	2.0	1.0
Grossular	38.6	0.3	23.8	30.5	30.1	1.6
Andradite	59.7	98.9	74.7	67.9	67.9	97.4

	85 Rim/Light	86 Core/Light	86 Dark/Rim	87 Core/Light	87 Rim/Dark	89 Core/Dark
CaO	32.47	33.57	33.47	32.08	32.96	33.50
MgO	0.09	0.07	0.07	0.08	0.05	0.03
TiO2	0.04	0.44	1.25	0.02	1.32	
SiO2	34.79	35.50	35.55	34.44	36.53	36.54
Al2O3	1.08	8.36	9.07	1.33	6.54	8.23
Fe2O3	28.55	20.37	17.25	28.21	22.41	19.77
MnO	0.39	0.70	0.75	0.60	0.74	0.75
Cr2O3			0.10			
Cl				0.03		
F	0.14	1.03	0.38	0.31	0.16	0.49
K2O			0.02	0.02	0.03	
P2O5	0.03	0.04	0.04	0.05	0.05	
Na2O			0.05	0.06	0.06	
BaO		0.04				
V2O3		0.08	0.19		0.06	
ZnO						
TOTAL	**97.57**	**99.80**	**98.08**	**97.13**	**100.92**	**99.18**

Formulae
$(Ca,Mg,Mn)_6(Fe,Al)_4Si_6O_{24}$

	85 Rim/Light	86 Core/Light	86 Dark/Rim	87 Core/Light	87 Rim/Dark	89 Core/Dark
Mg	0.022	0.016	0.016	0.018	0.013	0.009
Mn	0.049	0.099	0.109	0.086	0.107	0.108
Ca	5.746	5.937	5.752	5.772	5.958	6.004
Total	**5.817**	**6.052**	**5.877**	**5.876**	**6.078**	**6.121**
Fe	3.674	2.522	2.117	3.651	2.860	2.458
Al	0.273	1.513	1.600	0.299	1.402	1.456
Ti	0.006	0.045	0.136	0.004	0.152	
Cr			0.001			
Total	**3.953**	**4.08**	**3.854**	**3.954**	**4.414**	**3.914**
Si	5.974	5.812	5.865	5.913	5.850	5.874
Al	0.026	0.188	0.135	0.087	0.15	0.126
Total	**6.000**	**6.000**	**6.000**	**6.000**	**6.000**	**6.000**
Total	*15.77*	*16.132*	*15.731*	*15.83*	*16.492*	*16.035*
Spessartine	0.96	1.66	1.74	1.48	1.68	1.74
Grossular	5.37	35.96	41.81	6.45	29.30	36.42
Andradite	93.67	62.38	56.15	92.07	69.02	61.84

	89 Rim/Light	90 Core	90 Rim	91 Core/Light	91 Rim/Dark	93 Core
CaO	32.20	32.40	32.54	32.42	33.77	33.79
MgO		0.06	0.05	0.10	0.08	0.06
TiO2	0.02	0.26	0.02	0.03	0.19	1.71
SiO2	35.53	35.13	36.92	34.36	36.06	35.62
Al2O3		7.04	7.62	0.49	9.09	7.95
Fe2O3	30.90	21.50	20.75	30.12	19.01	18.75
MnO	0.55	0.65	0.70	0.45	0.77	0.82
Cr2O3						
Cl		0.03	0.02	0.02		
F	0.11	0.81	0.63	0.08	0.74	0.29
K2O		0.05	0.03	0.04	0.02	
P2O5	0.04	0.07	0.07		0.02	0.03
Na2O		0.08	0.07	0.05		
BaO				0.03		
V2O3			0.03		0.16	0.22
ZnO						
TOTAL	**99.36**	**97.75**	**99.21**	**98.22**	**99.64**	**99.21**

Formulae
$(Ca,Mg,Mn)_6(Fe,Al)_4Si_6O_{24}$

Mg	0.000	0.014	0.013	0.024	0.021	0.014
Mn	0.076	0.091	0.099	0.056	0.112	0.118
Ca	5.914	5.765	5.974	5.897	5.901	5.870
Total	**5.990**	**5.870**	**6.086**	**5.977**	**6.034**	**6.002**
Fe	3.914	2.621	2.587	3.808	2.355	2.327
Al		1.421	1.481	0.189	1.630	1.498
Ti	0.003	0.034	0.004	0.004	0.027	0.174
Cr						
Total	**3.917**	**4.076**	**4.072**	**4.001**	**4.012**	**3.999**
Si	5.936	5.900	5.876	5.967	5.869	5.834
Al	0.064	0.1	0.124	0.033	0.131	0.166
Total	**6.000**	**6.000**	**6.000**	**6.000**	**6.000**	**6.000**
Total	*15.907*	*15.946*	*16.158*	*15.978*	*16.046*	*16.001*
Spessartine	1.32	1.56	1.60	1.11	1.79	1.87
Grossular		31.25	34.21	2.66	39.48	36.81
Andradite	98.68	67.19	64.19	96.23	58.73	61.32

	93 Rim	99 Core/Light	99 Rim/Dark
CaO	33.26	32.93	32.24
MgO	0.04	0.05	0.07
TiO2	1.00		
SiO2	35.30	34.81	34.51
Al2O3	6.63	3.06	0.20
Fe2O3	21.99	27.13	30.14
MnO	0.69	0.55	0.52
Cr2O3			
Cl	0.02		
F	0.16	0.12	0.11
K2O	0.01		
P2O5			0.04
Na2O			0.04
BaO			
V2O3			
ZnO			0.07
TOTAL	**99.09**	**98.67**	**97.93**

Formulae
$(Ca,Mg,Mn)_6(Fe,Al)_4Si_6O_{24}$

	93 Rim	99 Core/Light	99 Rim/Dark
Mg	0.011	0.014	0.016
Mn	0.099	0.080	0.075
Ca	5.903	5.998	5.740
Total	**6.013**	**6.092**	**5.831**
Fe	2.785	3.344	3.801
Al	1.123	0.516	0.005
Ti	0.120		
Cr			
Total	**4.028**	**3.86**	**3.806**
Si	5.852	5.921	5.915
Al	0.148	0.079	0.085
Total	**6.000**	**6.000**	**6.000**
Total	*16.041*	*15.952*	*15.637*
Spessartine	1.62	1.34	1.27
Grossular	29.41	13.61	1.20
Andradite	68.97	85.06	97.53

Laser–Ablation Inductively–Coupled Mass Spectrometry (LA–ICP–MS)

LA–ICP–MS spot analysis was conducted as a series of transects across a garnet from 17

individual samples covering a range of 232.1m (276 spot analyses). The analyses were

conducted on the Agilent 7500cx ICP–Quadrupole Mass Spectrometer with attached UP–213

NdTag New Wave pulsed solid state laser (UP–213 New Wave). The laser operated at pulse

rates of 5Hz, 65% power level and fluence of 11J/cm^2. Spot size was uniform with a diameter

of 40µm for garnet samples and 50µm for reference materials. Data reduction was conducted

using Iolite software (Woodhead *et al.,* 2007), and sample reference materials were NIST–

610 (Jochum *et al.,* 2011) and GSD–1G (Jochum *et al.,* 2005). The following set of elements

were monitored: **Ag, Al, As, Au, Ca, Ce, Co, Cr, Cu, Dy, Er, Eu, Fe, Ga, Gd, Hf, Ho, K,**

La, Lu, Mg, Mn, Mo, Nb, Nd, Ni, P, Pb, Pr, Sb, Sc, Se, Si, Sm, Sn, Tb, Th, Ti, Tm, U, V,

W, Y, Zn, Zr. Isotopes monitored: **Pb^{206}, Pb^{207}, Pb^{208}.** All analyses were conducted for 90

seconds, comprising of 30 second background measurements (laser off) and 60 second

sample analysis (laser on). Internal calibration was achieved using Ca concentration values

obtained from the EMPA. REE+Y data was chondrite normalised according to McDonough

& Sun (1995) (Table 5).

Table 5: Chondrite values used to normalise LA–ICP–MS data for REE+Y (McDonough & Sun, 1995)

La	0.237
Ce	0.613
Pr	0.0928
Nd	0.457
Sm	0.148
Eu	0.0563
Gd	0.199
Tb	0.0361
Dy	0.246
Y	1.57
Ho	0.0546
Er	0.16
Tm	0.0247
Yb	0.161
Lu	0.0246

P, K, Sc, Ti, V and Cr vs. Depth

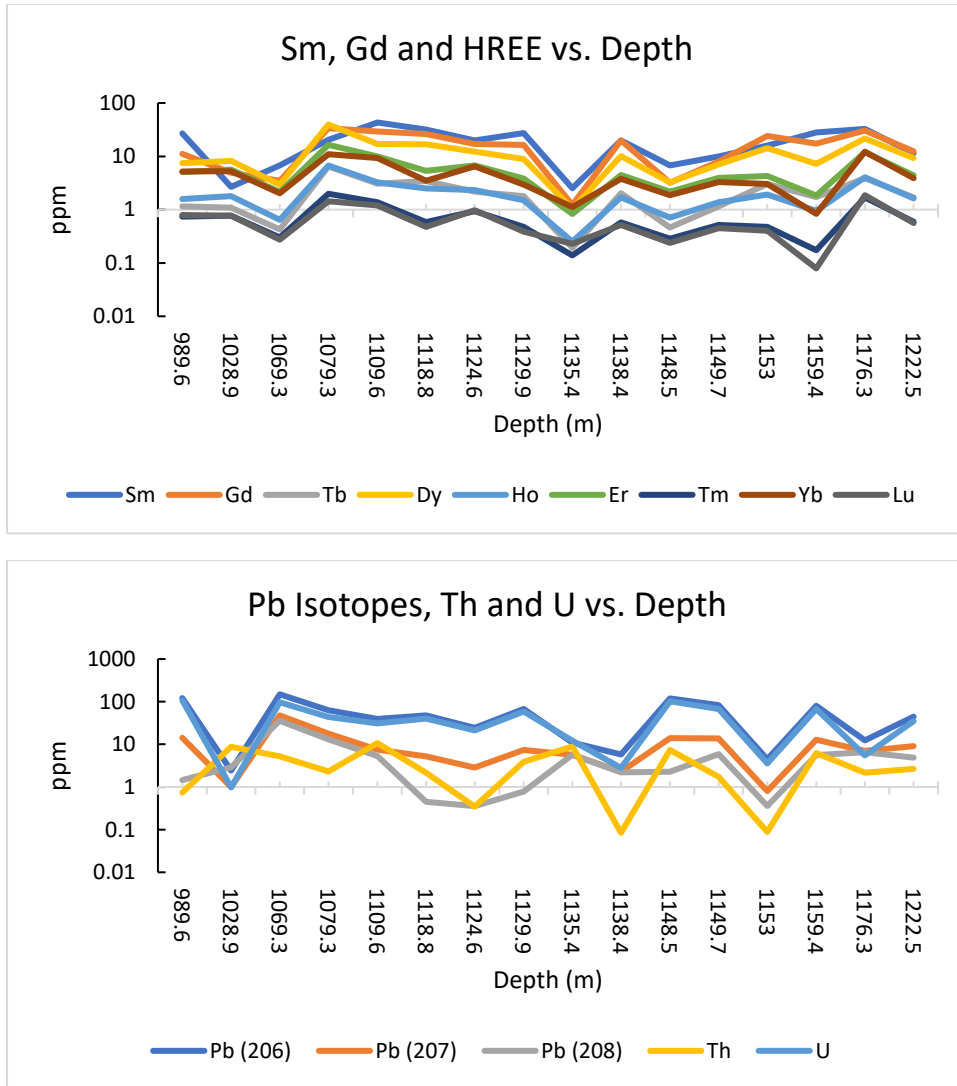Co, Ni, Cu and Zn vs. Depth

La, Ce, Pr and Nd vs. Depth
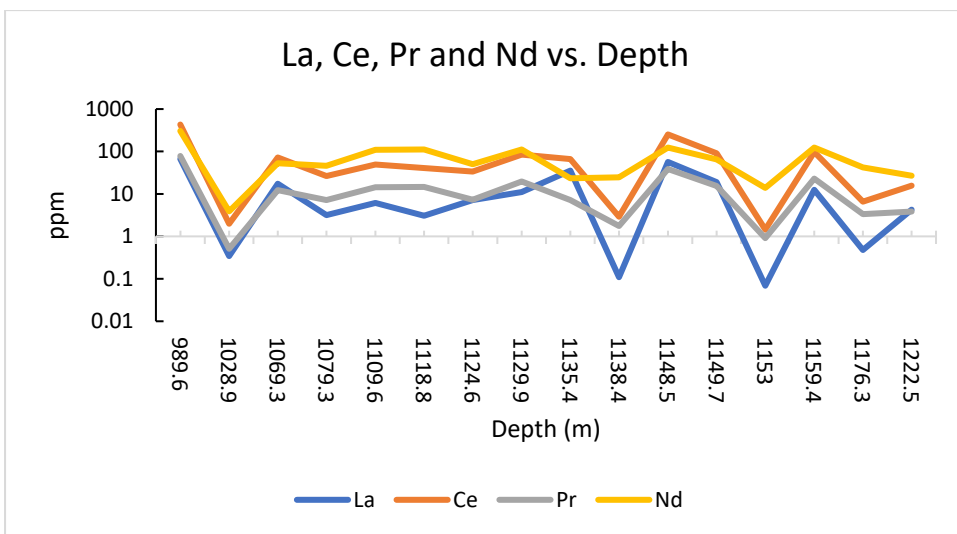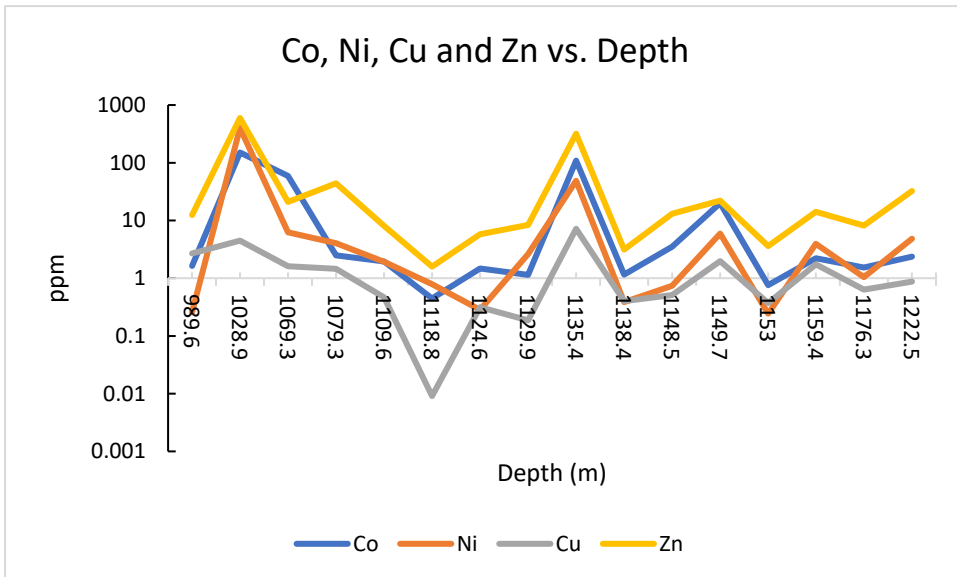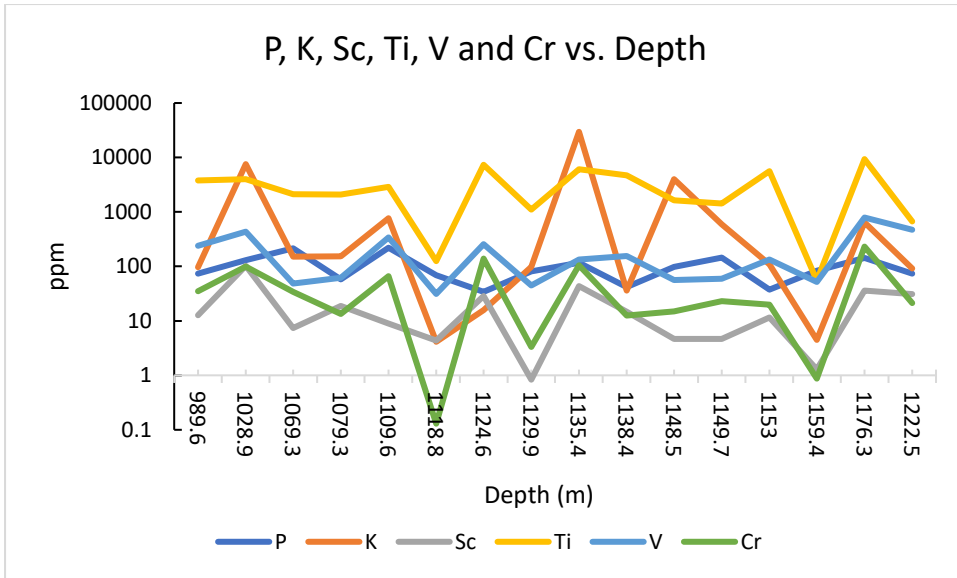
Figure 18: LA–ICP–MS spot data (average of values from garnet transect) as a function of depth. No elements show any correlation to mineralisation (Figure 3).

Table 6: LA-ICP-MS spot data (average of transect) for each garnet sample.

Garnet ID	65	71	77	78	82	83	84	85	86	87	88	89	90	91	93	99
Depth	989.6	1028.9	1069.3	1079.3	1109.6	1118.8	1124.6	1129.9	1135.4	1138.4	1148.5	1149.7	1153	1159.4	1176.3	1222.5
Ca	395706.3	136495.2	352244.4	343888.9	311855.2	411842.9	359750	341500	133831.6	322700	410986.7	338157.9	274966.7	418647.1	442323.5	443750
Mg	496.8813	372300	2766.581	21571.18	844.7448	441.5667	566.175	1074.479	112073.7	277.4522	475.6333	3157.484	483.94	1294.088	477.5941	3592.6
Al	19235.5	83504.76	38937.04	36985	53054.14	4963.381	50006.5	28333.82	73289.47	52754.78	25272.47	53294.21	54406	15568.56	56853.53	27106.4
Si	251637.5	932333.3	234959.3	240333.3	236703.4	237295.2	237000	237294.1	1462000	232804.3	312533.3	246157.9	236766.7	243058.8	243858.8	242820
P	73.95	129.4286	213.4815	58	220.2414	69.26667	34.125	81.11765	117.3158	42.01739	97.73333	145.7895	37.73333	82.76471	144	73.25
K	96.93125	7531.714	150.3815	153.0667	763.569	4.128571	15.855	98.42059	29586.32	35.84348	3997.78	594.3684	109.4667	4.5	645.3235	91.65
Sc	12.67288	102.4571	7.421481	18.67917	8.918621	4.351667	28.5265	0.832676	43.29474	14.71913	4.6404	4.691579	11.48	1.280353	35.94059	30.9665
Ti	3766.869	3972.667	2111.037	2086.128	2871	124.9424	7320.05	1101.179	6094.563	4700.87	1624.613	1430.179	5595.8	54.90941	9331.941	671.995
V	238.1338	434.0762	48.48185	61.84611	340.4931	31.22238	257.748	44.55588	133.2105	154.5739	56.058	59.38042	133.6467	51.56294	789.6529	470.51
Cr	35.21438	99.80476	33.96074	13.38722	66.59241	0.129524	138.898	3.313529	104.8842	12.52391	14.966	22.92684	19.9	0.872941	231.0488	21.345
Mn	6233.938	18097.14	8240	6370	7032.069	4348.905	7832	5629.471	29444.74	8282.609	6419.533	8089.526	8765.333	6163.059	8353.588	6170.75
Fe	274731.3	253947.6	229144.4	238777.8	211479.3	303166.7	208250	251676.5	569315.8	207426.1	266633.3	227842.1	215253.3	279823.5	191641.2	263135
Co	1.628875	150.581	59.33004	2.479944	1.957655	0.445571	1.46985	1.136382	109.5789	1.163696	3.498667	19.84211	0.754133	2.212353	1.529235	2.37
Ni	0.260688	400.9048	6.268148	4.051111	1.915862	0.786571	0.28445	2.624706	49.03684	0.386304	0.735267	5.893158	0.243333	3.937647	1.048824	4.821
Cu	2.68	4.496667	1.609889	1.456111	0.467345	0.009095	0.3145	0.186471	7.181053	0.402609	0.512067	1.977895	0.373333	1.746471	0.636706	0.87485
Zn	12.4575	596.0952	21.09	43.96333	8.006552	1.588095	5.7435	8.38	319.8947	3.111304	13.08533	22.20053	3.604	14.04176	8.161765	32.5705
Ga (69)	55.41875	60.15714	19.2937	23.51667	96.90345	70.54286	36.9185	44.06941	47.3	40.96957	17.706	23.53263	44.55333	41.95647	48.2	53.086
Ga (71)	60.6	56.37619	20.03222	24.15	92.03448	71.28095	37.124	44.56882	43.63789	42.18261	16.61067	23.58526	45.97333	42.87059	48.43529	53.636
As	298.1719	11.22857	1025.015	294.9278	115.3097	208.8248	79.066	396.2176	6.5	1.916957	459.1267	263.4579	2.396	492.7647	6.181765	507.92
Se	2.50375	0	0.62037	1.731667	3.038621	2.975714	1.302	1.953235	0.121053	1.709565	0.295333	0.556842	0.913333	2.137059	2.987059	0.986
Y	43.28188	53.30381	20.14407	199.1317	92.44448	72.09662	65.471	40.43824	6.924211	46.55261	20.44707	45.09868	52.30267	24.65942	109.9629	44.587
Zr	74.8575	63.3619	46.79852	60.03772	98.29138	2.050714	143.6325	23.76294	255.9526	99.01391	42.47	59.26826	68.66667	3.513294	107.4353	14.03385
Nb	26.2705	9.182857	9.12963	9.852389	32.23345	1.747581	35.2045	13.04721	33.16095	76.99565	6.487573	7.117432	68.30667	0.807324	49.62706	3.49475
Mo	1.44075	0.236619	1.354333	0.872389	0.512931	0.319476	0.3565	1.021765	0.826053	0.130348	1.738	1.121211	0.102467	1.401941	0.180353	0.2474
Ag	0.01375	0.01	0.168111	0.045222	0.010276	0	0	0.010265	0.108579	0	0.0126	0.059	0.022733	0.002	0.014294	0.0045
Sn	200.1913	12.81095	32.66222	11.11	49.8	176.1762	36.0945	40.83588	9.928421	41.78261	13.35	20.62368	59.03333	31.22941	25.25294	104.105
Sb	0.289313	5.632381	11.20519	0.403556	0.936276	0.047905	0.2499	0.948971	7.774211	0.082748	1.9562	1.349947	0.020733	0.264471	0.360706	0.34225
La	66.90575	0.345429	17.43926	3.188333	6.11469	3.043571	7.12938	11.14788	0.109939	56.36533	19.13668	0.068793	12.54724	0.479647	4.2482
Ce	432.1138	1.981714	72.35074	26.22556	49.63931	40.59095	33.56475	84.24265	66.19737	2.927435	254.5667	90.62158	1.448933	97.72471	6.526882	15.71455
Pr	78.39313	0.510143	12.3537	7.157222	14.30138	14.69286	7.28615	19.75353	7.130474	1.744565	38.562	15.42105	0.912333	22.93941	3.339706	3.83285
Nd	305.3625	3.888095	52.74741	46.28167	110.0562	110.6662	50.034	111.7647	23.44316	24.75522	124.58	65.19526	13.908	123.6176	42	26.6505
Sm	26.88188	2.68619	6.787407	20.52	43.14483	31.78762	19.9045	27.31265	2.523053	19.97696	6.750667	9.996842	16.03067	27.94235	32.76412	11.4435
Eu	10.45688	0.686286	7.638889	7.414444	9.351034	18.34762	4.871	10.95471	0.376526	4.005217	6.195333	6.740526	3.824667	10.86176	5.922765	8.8065
Gd	11.12375	4.945238	3.473704	33.80056	29.38172	26.28762	17.1155	16.42912	1.223789	19.82217	3.194	7.937895	24.08333	17.19365	30.36059	12.4585
Tb	1.156375	1.091286	0.422889	6.450944	3.093621	3.452095	2.18545	1.791382	0.191421	2.016391	0.460867	1.144342	3.044867	1.727435	3.886941	1.70225
Dy	7.43475	8.160952	2.955556	39.52128	17.1131	16.83419	12.3275	8.955471	1.035684	10.04565	3.241533	7.053368	14.252	7.235353	21.72353	9.2258
Ho	1.590725	1.792762	0.647519	6.729111	3.259448	2.4903	2.32555	1.504176	0.251632	1.700087	0.7056	1.373979	1.9308	0.944771	4.053176	1.63705
Er	5.0675	5.671429	2.149889	16.42017	9.95069	5.336476	6.7554	3.848265	0.828737	4.486522	2.1704	3.915263	4.273333	1.842682	11.93765	4.42905
Tm	0.740244	0.76981	0.301756	1.986311	1.375931	0.587586	0.93405	0.476971	0.138721	0.577913	0.286073	0.5134	0.473667	0.172276	1.692824	0.59085
Yb	5.199688	5.283333	2.041259	10.98317	9.333793	3.466905	6.463	2.957441	1.120421	3.786522	1.862733	3.293789	3.031333	0.834471	12.23176	3.862
Lu	0.792125	0.768143	0.273415	1.43075	1.195759	0.474576	0.96935	0.386265	0.227316	0.519478	0.237953	0.446668	0.400867	0.079012	1.865882	0.56215
Hf	3.603625	2.433333	1.54537	2.224556	3.192345	0.045587	7.1968	0.809647	7.930526	0.186957	1.381133	2.034316	2.502667	0.064	6.489059	0.60445
W	507.4713	0.262571	461.7259	391.6911	168.0034	265.5952	89.3335	305.1206	3.023421	0.100826	684.2	351.2316	0.175067	430.6353	1.965882	281.7255
Au	0	0	0.019759	0.000922	0.002793	0	0	0.000618	0.005	0.002696	0	0.005211	0.001133	0	0	0
Pb (206)	121.1506	2.426667	148.6815	63.02833	39.38276	47.56667	24.2605	67.55118	10.96526	5.77087	119.8067	82.57368	4.486	80.34118	12.45118	44.7805
Pb (207)	14.27875	0.987143	47.60111	17.87611	7.485517	5.200048	2.87605	7.422647	5.700526	2.269913	14.01467	13.65737	0.802533	12.85706	6.955294	9.011
Pb (208)	1.456313	2.878571	35.59333	13.16033	5.341724	0.445476	0.35645	0.779647	5.676316	2.208826	2.273	5.884368	0.357333	5.623471	6.523471	4.8734
Th	0.737	8.804286	5.25763	2.324167	10.67	2.147905	0.34445	3.914461	8.987368	0.084348	7.394667	1.734526	0.088333	6.258271	2.157765	2.6636
U	107.5819	0.97581	96.48148	44.05222	31.04207	40.06571	21.135	58.28382	12.07947	2.796087	101.9467	67.38895	3.568667	67.27529	5.545294	35.166

LA–ICP–MS element distribution maps

LA–ICP–MS element distribution maps were conducted on the Agilent 7500cx ICP–Quadrupole Mass Spectrometer with attached UP–213 NdTag New Wave pulsed solid state laser (UP–213 New Wave). The laser operated at pulse rates of 5Hz, 65% power level and fluence of 11J/cm^2. The sample reference material was GSD–1G (Jochum *et al.,* 2005). The following set of elements were monitored: **Ag, Al, As, Au, Ca, Ce, Co, Cr, Cu, Dy, Er, Eu, Fe, Gd, Hf, Ho, K, La, Lu, Mg, Mn, Mo, Nb, Nd, Ni, P, Pb, Pr, Sb, Sc, Se, Si, Sm, Sn, Tb, Th, Ti, Tm, U, V, W, Y, Zn, Zr.** Isotopes monitored: **Ga^{69}, Ga^{71}, Pb^{206}, Pb^{207}, Pb^{208}**. Internal calibration was achieved using Ca concentration values obtained from the EMPA. The laser operated at pulse rates of 5Hz, 70% power level and fluence of 11J/cm^2. Spot size was uniform with a diameter of 50µm for reference materials, but varied for each garnet depending on map detail and grain size. Images were obtained via ablating parallel line raster, with spacing between lines equal to the size of the beam used, and a scan speed of double the beam. 30 seconds background acquisition was acquired at the start of each raster, with a 15 second delay afterwards. Typically mapping was conducted over 10–14 hours of which instrument drift could occur; which was corrected via reference sample material assessment between each garnet grain, and then applying a line of best fit to adjust data. Data reduction was conducted using Iolite software (Woodhead *et al.,* 2007).
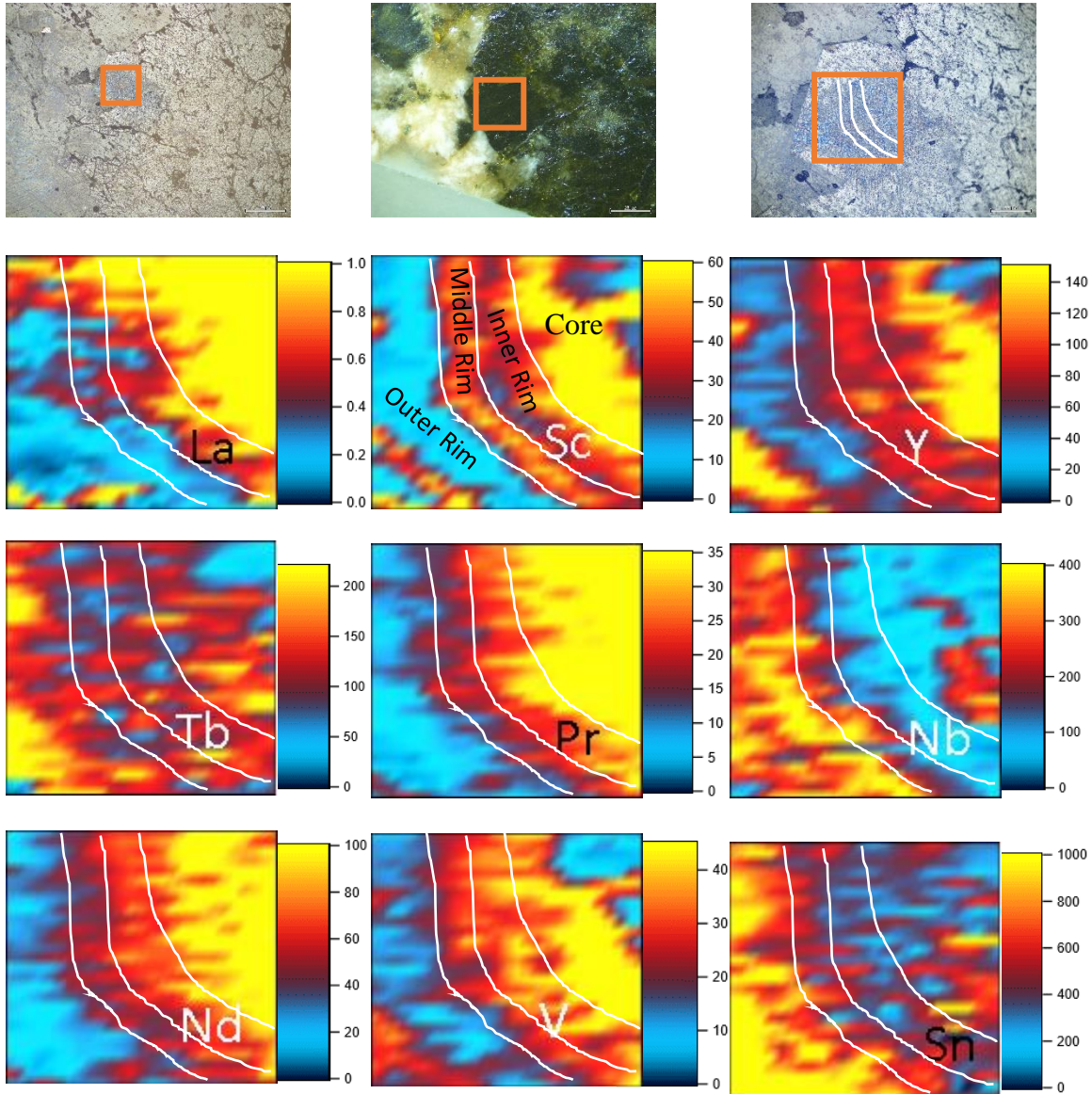
Figure 19: LA–ICP–MS element distribution map of elements of interest for garnet 84. The orange box represents where the map occurred, the white lines define oscillatory zoning.
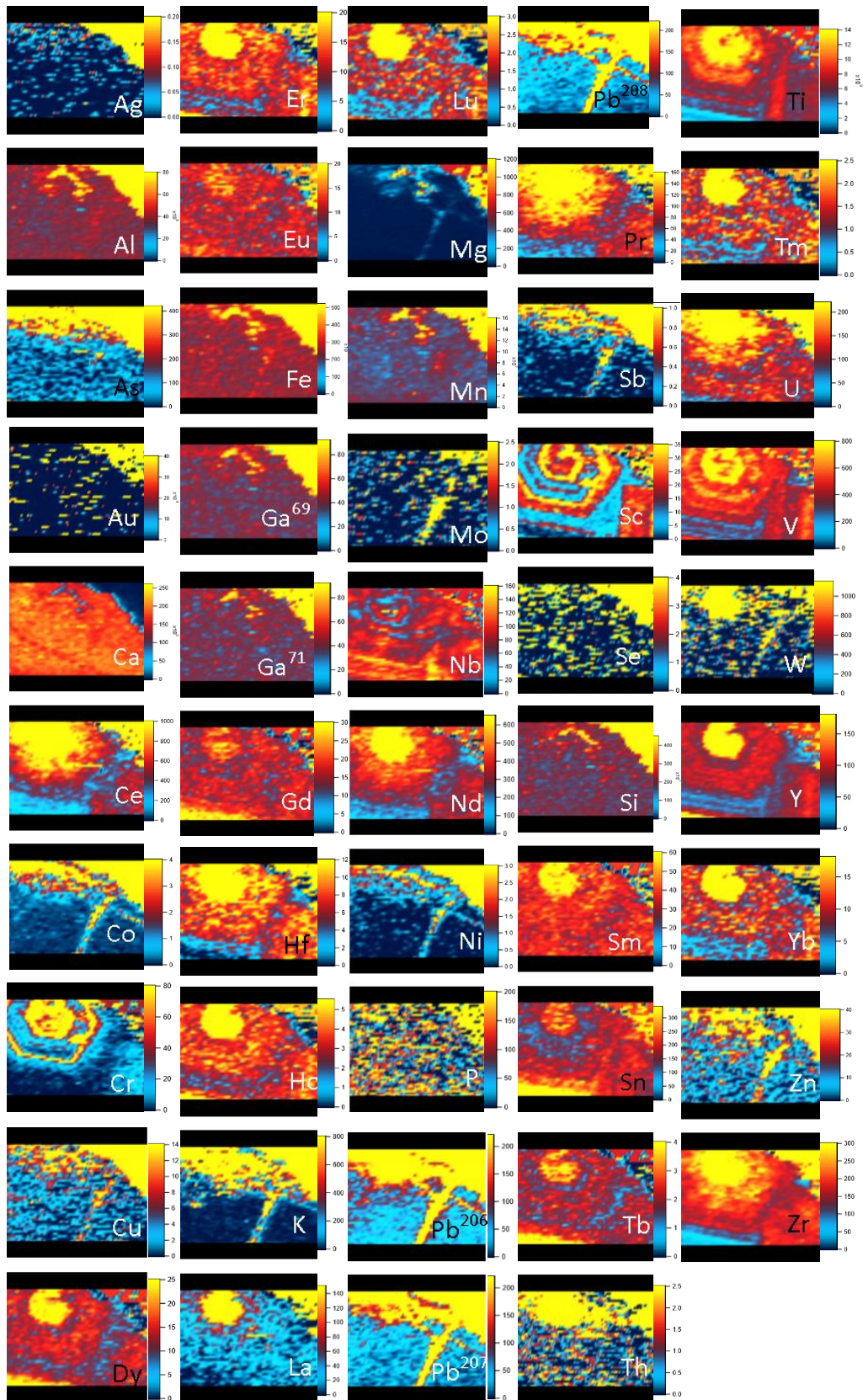
Figure 20: LA–ICP–MS element distribution maps for garnet 87. Grain boundaries and zonation is highlighted in figure 10.
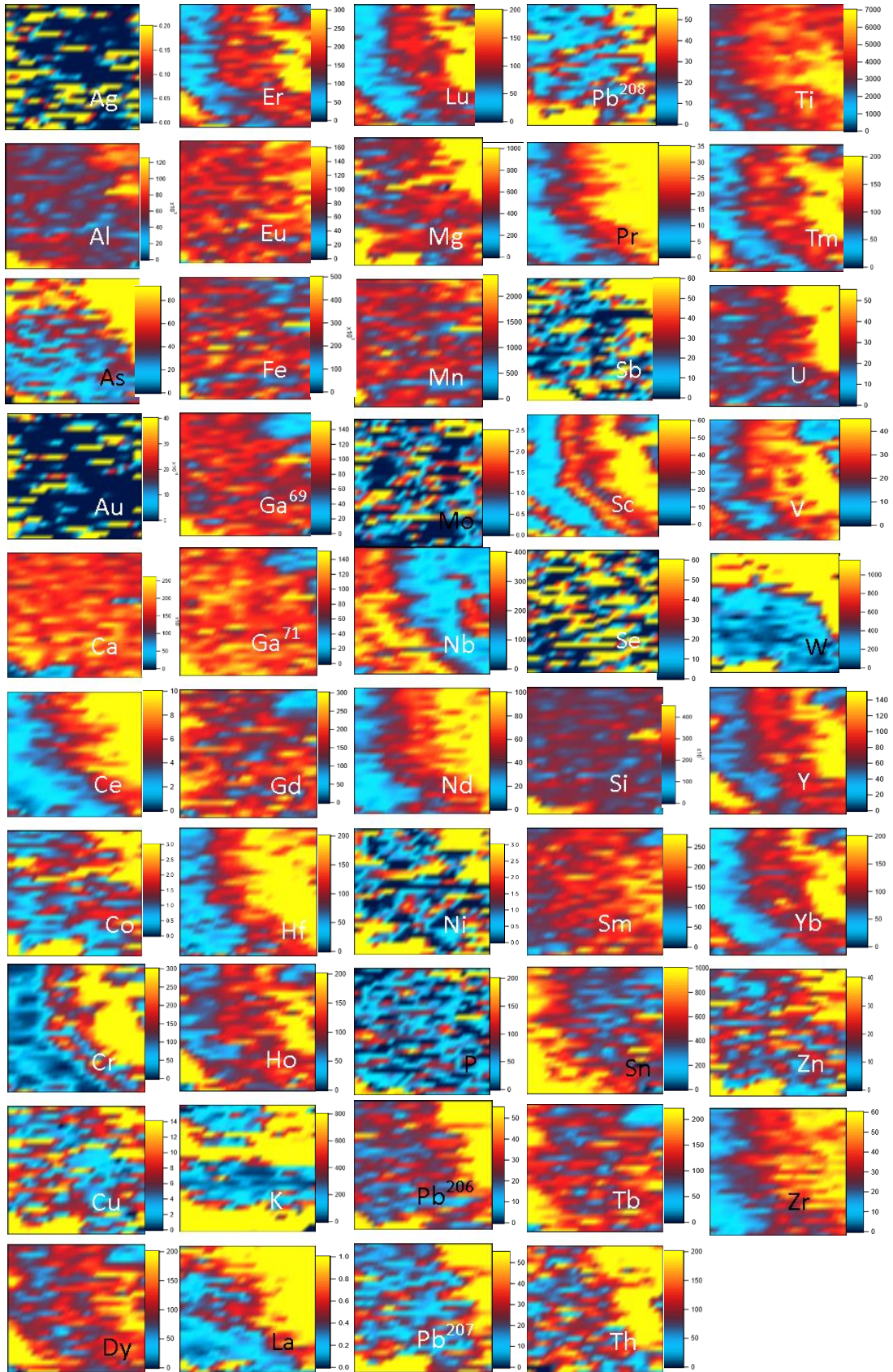
Figure 21: LA–ICP–MS element distribution maps for garnet 84. Grain boundaries and zonation is highlighted in figure 20.
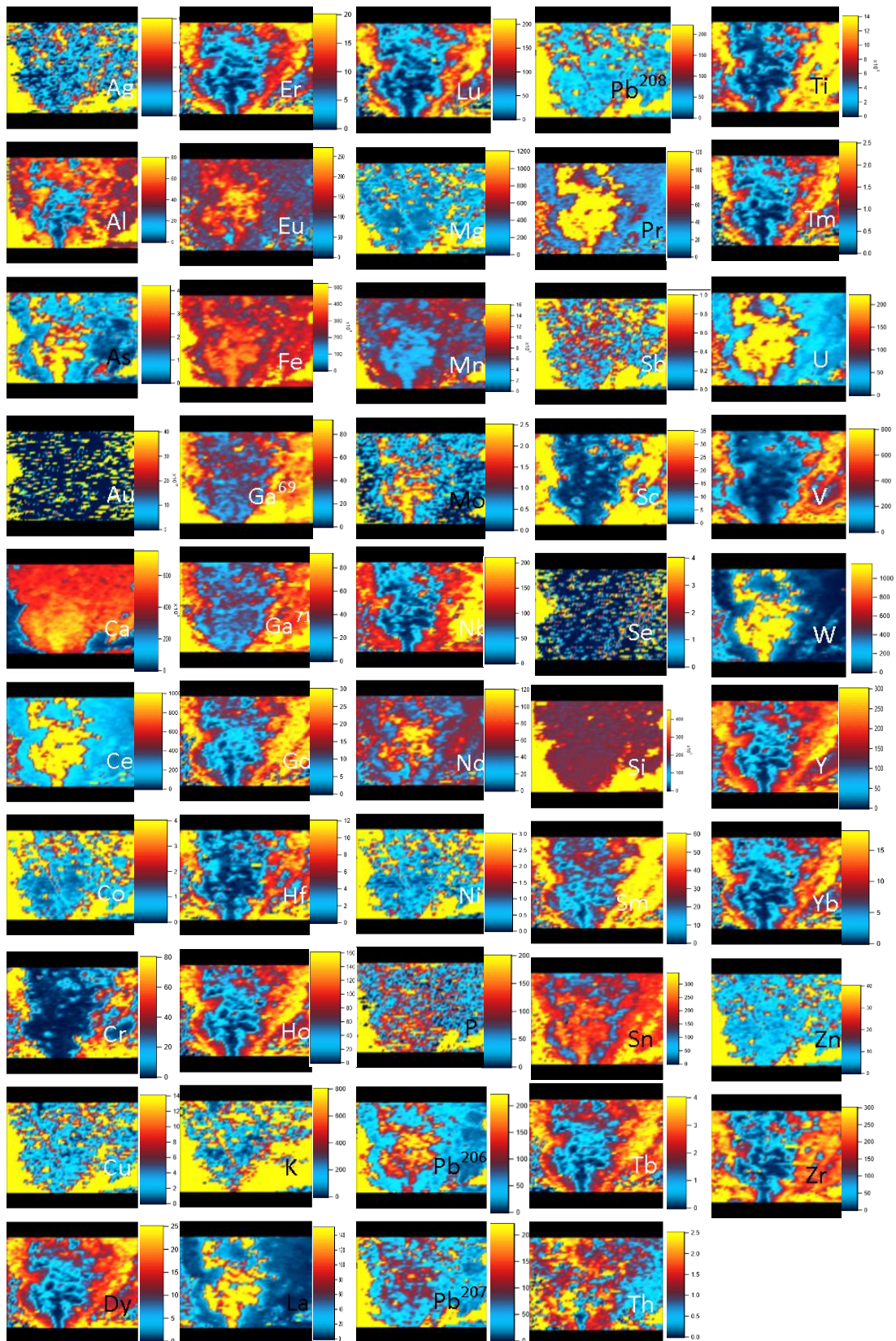
Figure 22: LA–ICP–MS element distribution maps for garnet 89. Grain boundaries and zonation is highlighted in figure 11.
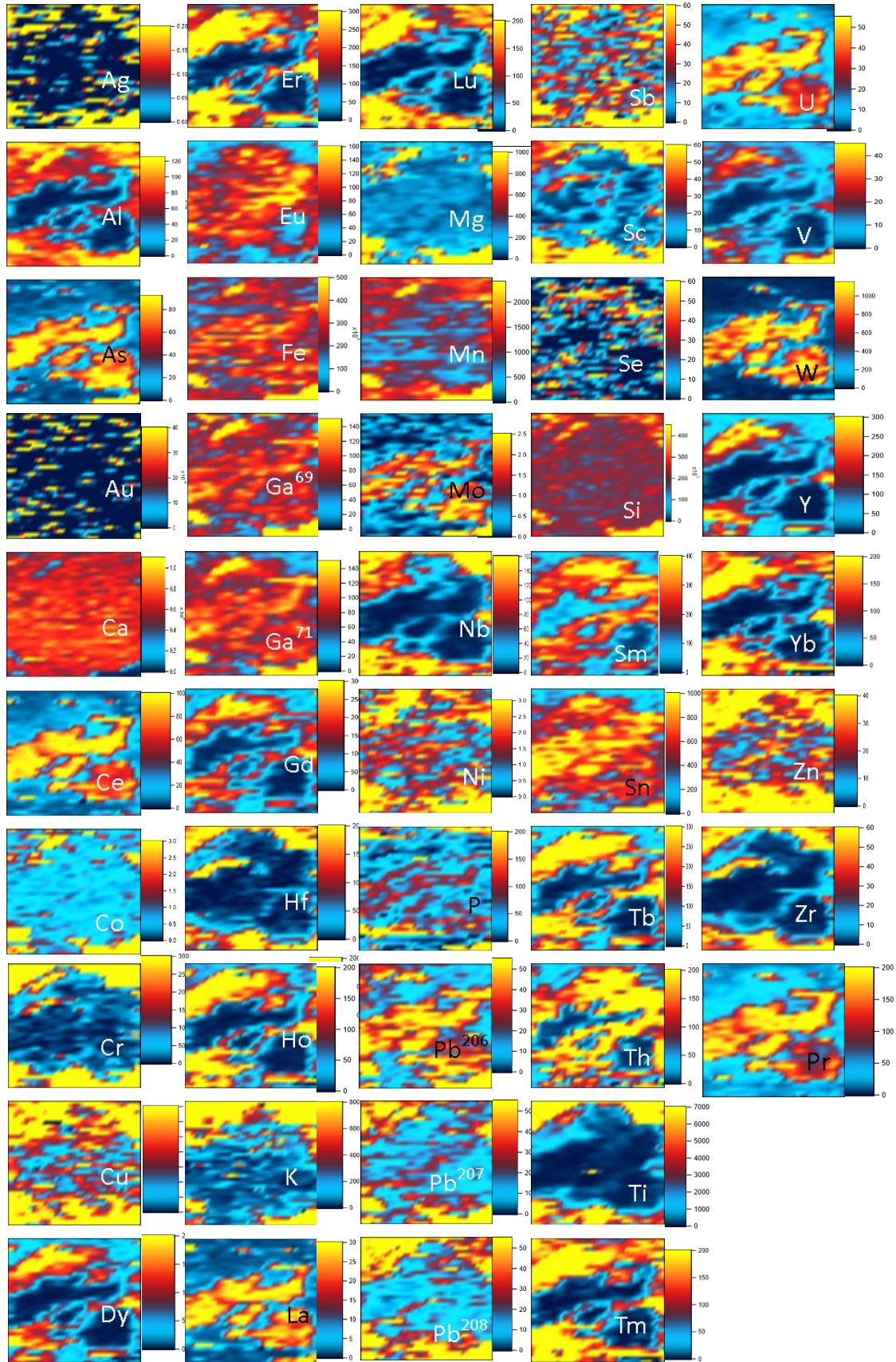
Figure 23: LA–ICP–MS element distribution maps for garnet 91. Grain boundaries and zonation is highlighted in figure 12.

Whole rock geochemistry

Geochemical data for the SAR8 drill hole was gathered via. DMITRE and Monax Mining Limited from 2007 to 2016 and collated by Fabris (2016). These analysis were conducted by Intertek Genalysis Laboratory Services, Adelaide. Homogeneous sub-sampling of each location was undertaken, and pulverised with quartz washes inbetween, minimising contamination risk. Analyses of standards and duplicates were routinely performed to create an acceptable error range. The determination techniques undertaken are given in Table 7.

Table 7: Determination techniques used by Fabris (2016) for each element/oxide.

Lithium borate fusion, ICP–OES determination		Four acid digests, ICP–OES determination.	Lead collection fire assay 25g charge, ICP–MS determination.	Carbonate fusion, Selective Ion Electrode determination
SiO2	Y	S	Au	F
Fe2O3	Ga	Cu	Pd	
CaO	Sn	As	Pt	
Al2O3	U	Co		
K2O	Sc	Zn		
MgO	Sm	Ni		
MnO	Pr	Pb		
Na2O	Gd	Mo		
P2O5	Hf	Li		
TiO2	Dy	Cs		
Ba	Er	Sb		
Rb	Yb	Nb		
Zr	Eu	Se		
V	Be	Ag		
Sr	Ho	Tl		
Ce	Ta	Bi		
Cr	Tb	Te		
Nd	Tm	In		
W	Lu	Ge		
La		Cd		
Th		Re		